coasts

MDPI

Article

Coupled BEM-FEM Fracture Response Analysis of Concrete Gravity Seawall Under Sea-Level Rise and Crack-Face Hydrostatic Pressure

Raja Chandrika Revella [1], Surya Teja Gollapalli [1] and Madasamy Arockiasamy [1,2,*]

[1] Department of Civil, Environmental and Geomatics Engineering, Florida Atlantic University, Boca Raton, FL 33431-0991, USA; rrevella2023@fau.edu (R.C.R.); sgollapalli2023@fau.edu (S.T.G.)
[2] Center for Infrastructure and Constructed Facilities, Department of Civil, Environmental and Geomatics Engineering, Florida Atlantic University, Boca Raton, FL 33431-0991, USA
* Correspondence: arockias@fau.edu

Abstract

Aging concrete seawalls are increasingly exposed to deterioration and sea-level-rise (SLR)-related hydraulic demands, yet the fracture response of pre-existing water-accessible cracks under combined coastal loading remains insufficiently understood. A MATLAB R2025a-based coupled BEM-FEM framework is developed to evaluate a plain-concrete gravity seawall using linear-elastic fracture mechanics (LEFM) under plane-strain conditions. Quadratic boundary elements represent the uncracked seawall region, while a locally refined Q8 FEM patch with quarter-point elements represents the toe-crack response. Parametric analyses consider self-weight, 25% and 50% backfill-pressure reductions, seawater levels of 1.52, 1.82, and 3.05 m, crack-face hydrostatic pressure, and normalized crack lengths, a/W = 0.1–0.7. Benchmark and mesh-sensitivity studies demonstrate stable fracture parameters. Results show that a/W primarily governs the nonlinear increase in fracture response, whereas crack-face hydrostatic pressure reduces both the closure tendency and the J-integral-based equivalent stress-intensity magnitude, K_J. Elevated seawater levels and backfill reduction exert secondary influences. The toughness-normalized index remains below unity, and crack-face displacement is normal-component-dominant. Independent ANSYS 2021R1 analyses provide trend-level corroboration of reduced equivalent fracture magnitude and closure-directed displacement. Overall, the coupled BEM-FEM framework identifies crack length and assumed concrete fracture toughness as governing parameters for the screened response and provides an efficient numerical approach for coastal concrete fracture assessment.

Keywords: coupled BEM-FEM; plain-concrete gravity seawall; linear-elastic fracture mechanics (LEFM); sea-level rise (SLR); normalized crack lengths; crack-face hydrostatic pressure; J-integral-based equivalent stress-intensity magnitude; crack-face displacement; toughness-normalized index; MATLAB

Academic Editors: Guang Yin, Wengang Qi and Muk Chen Ong

Received: 5 September 2026
Revised: 24 October 2026
Accepted: 29 October 2026
Published: 4 November 2026

Copyright: © 2026 by the authors. Licensee MDPI, Basel, Switzerland. This article is an open access article distributed under the terms and conditions of the Creative Commons Attribution (CC BY) license.

1. Introduction

Coastal protection systems such as seawalls, bulkheads, and revetments are widely used to reduce erosion, flooding, and wave damage in developed shoreline areas. Concrete gravity seawalls are especially common because they rely on their own weight and

base resistance for stability [1]. However, many seawalls are now deteriorating due to exposure to saline seawater, cycles of wetting and drying, wave forces, storm surges, erosion, and foundation problems. Recent studies highlight corrosion, cracking, durability loss, uncertain loads, and delayed maintenance as key issues for concrete seawalls [2]. USACE guidance also lists toe scour, undermining, overtopping, flanking, rotational sliding, and reinforcement corrosion as common types of seawall damage or failure [3]. These problems show that both overall stability and local material damage need to be considered when assessing older seawalls. Figure 1 shows the effect of deterioration and instability in an existing coastal protection wall.



Figure 1. Failed coastal protection wall rotating seaward in Volusia County, Florida (Zone VE). Adapted from Figure 3-34 of FEMA P-2342 [4]. Credit: Federal Emergency Management Agency (FEMA), U.S. Department of Homeland Security, 2023. U.S. Government work [4].

The vulnerability of coastal infrastructure is increasing as seawalls age and hydraulic demand intensifies due to sea-level rise and more frequent coastal storms [5]. NOAA projects an additional 0.254 to 0.304 m of sea-level rise along the U.S. coastline by the year 2050 [6], while long-term observations indicate a global mean sea-level increase of approximately 8–9 inches since 1880 [7]. Regional observations along the Georgia Bight, including northeast Florida, also indicate acceleration in relative sea-level-rise rates from historical values of approximately 3.6 ± 0.2 mm/year to about 9.8 ± 0.3 mm/year during 2003–2022 [8]. Accordingly, USACE guidance recommends incorporating projected sea-level scenarios into the planning, design, operation, maintenance, and rehabilitation of coastal infrastructure [9].

Conventional assessments primarily address global stability through checks such as sliding, overturning, bearing capacity, scour, and seabed deformation [10]. These evaluations are necessary but do not directly quantify the localized response of an existing crack. When seawater penetrates a water-accessible crack, hydrostatic pressure develops across the opposing crack faces and acts locally in the direction of crack opening [11].

As a result, a cracked seawall may meet global equilibrium requirements while still experiencing local fracture demand due to tensile stress, crack-face water pressure, or erosion-induced stress redistribution. Fracture mechanics offers an appropriate framework for evaluating concrete cracking by considering energy release, strain softening, size effects, and progressive fracture rather than simple stress exceedance [12]. Fracture-based assessment of a concrete seawall requires evaluating stress-intensity factors (SIFs), the J-

integral (J), and crack-opening displacement (COD) to quantify crack-tip demand, energy release, and crack-opening response using linear elastic fracture mechanics (LEFM). In linear-elastic fracture mechanics, crack deformation is commonly classified into three basic fracture modes, shown in Figure 2.

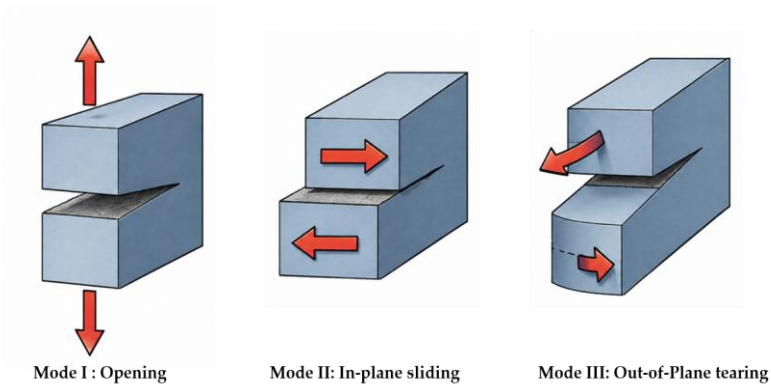


Figure 2. Basic fracture modes showing the relative displacement of crack faces: Mode I, opening mode with crack faces separating normal to the crack plane; Mode II, in-plane shear mode with opposite sliding displacement parallel to the crack plane; and Mode III, out-of-plane shear mode with tearing displacement perpendicular to the in-plane crack front.

USACE guidance similarly recognizes the structural relevance of water-filled cracks in concrete hydraulic infrastructure [13,14]. Therefore, a pre-existing water-accessible crack represents a mechanically meaningful condition for fracture-based assessment of aging seawalls.

Numerical methods are commonly used in fracture mechanics because it is difficult to calculate crack-tip stresses, crack opening, and energy release analytically for concrete structures with complex shapes. Ulfkjær [15] pointed out that concrete fracture often requires the finite element method (FEM) or the boundary element method (BEM), since analytical solutions typically apply only to simple shapes. In hydraulic concrete structures, Loarte et al. [11] used ABAQUS-based finite element analysis to show that internal water pressure can promote crack growth by following the crack extension, thereby reducing the pressure required to open a new crack. Experimental studies by Zhao et al. [16] confirm that water pressure acting on the faces of concrete cracks promotes crack opening and accelerates crack propagation. More recently, Hakimzadeh et al. [17] emphasized the importance of distinguishing crack-normal opening, tangential sliding, crack-parallel deformation, and crack-face contact in numerical fracture models. This study supports the explicit representation of both crack faces when evaluating hydraulically loaded, pre-existing cracks. Similarly, Siva Parvathi et al. [18] used the ANSYS-based FEM followed by the extended finite element method (XFEM) to analyze a concrete gravity dam and found that stress-intensity factor, K_I, increases with crack length until the material fracture toughness is reached. More recently, Ramadan et al. [19] showed that factors such as weak layers, hydraulic fracture risk, mixed-mode crack growth, and crack location in concrete gravity dams can all be modeled using FEM and fracture mechanics. Wu et al. [20] showed that crack mouth opening displacements (CMOD), crack mouth sliding displacements (CMSD), peak load, and crack paths can be predicted using FEM-based mixed-mode I–II fracture analysis. Silarom et al. [21] found that scour and backfill outflow can lower the protective ability and stability of coastal structures, as erosion-related support loss changes stresses and raises local fracture demand. Rambabu et al. [22] studied hydrodynamic pressures on vertical seawalls with submerged breakwaters using a numerical wave tank based on computational fluid dynamics (CFD). Their study shows the

importance of measuring changes in hydraulic pressure on seawalls as coastal conditions change, although it did not examine crack formation or stress intensity.

Using a coupled boundary element-finite element method (BEM-FEM) is an efficient way to assess fracture. Miyazaki et al. [23] introduced a BEM-FEM approach in which finite elements are used only near the crack tip, and boundary elements model the rest of the structure, achieving stress-intensity-factor accuracy better than 1% for several two-dimensional crack problems. Aour et al. [24] suggested that combining FEM near the crack tip with BEM in the surrounding area can accurately compute stress-intensity factors with fewer degrees of freedom. Su et al. [25] developed a spline fictitious boundary element method (SFBEM-FEM) coupling method in which the area near the crack is modeled as a BEM-based cracked super-element within a standard FEM mesh, enabling accurate stress-intensity calculations without requiring very fine FEM meshes around cracks. Zhang et al. [26] showed that using FEM for the whole structure and BEM for the crack region can reduce remeshing while still giving accurate SIF results during crack growth. Recent studies by Zhou et al. [27] on symmetric positive-definite BEM-FEM coupling show that BEM's nonlocal modeling and FEM's local detail can be combined in a stable way. Mukhtar et al. [28] also reviewed concrete fracture models and noted that accurate fracture simulation remains difficult due to stress singularities, fracture process zones, material heterogeneity, and complex shapes.

Concrete, however, is a quasi-brittle material in which a finite fracture process zone (FPZ) develops ahead of the crack tip. Consequently, LEFM does not explicitly represent tensile softening, distributed microcracking, aggregate bridging, or FPZ evolution. Bažant and Planas [29] showed that the applicability of LEFM depends on the size of the nonlinear fracture zone relative to the characteristic dimensions of the structure. For massive concrete gravity structures, the FPZ may be small relative to the overall structural dimensions, allowing LEFM to provide a useful engineering approximation under appropriate conditions [30].

To the authors' knowledge, limited published research has addressed the combined fracture response of a toe-cracked gravity seawall subjected to sea-level rise, erosion-induced reduction in backfill support, and internal crack-face hydrostatic pressure within a coupled BEM-FEM framework. This combined condition is significant because it connects climate-driven macro-environmental changes, such as sea-level rise and backfill support reduction, with local crack-driving mechanisms.

This study presents and validates a MATLAB-based coupled BEM-FEM framework for evaluating the fracture response of a plain-concrete gravity seawall containing a pre-existing seaward toe edge crack. The seawall is subjected to sea-level rise, erosion-induced backfill reduction, self-weight, and hydrostatic pressure acting on the crack faces. A local Q8 FEM crack patch resolves the near-tip displacement, strain, and stress fields, while the BEM represents the surrounding seawall through boundary-only discretization. The parametric analysis considers different normalized crack lengths (a/W) and coastal loading scenarios. The principal response measures, including (i) the normal and tangential crack-face displacement jumps, COD_y and COD_x, (ii) maximum normal displacement-jump magnitude, $|COD_y|_{max}$, (iii) J-integral-based equivalent stress-intensity magnitude, K_J, (iv) mode-dominance ratio, R_{COD}, and (v) the toughness-normalized index, K_J/K_{IC}, provide complementary information. The coupled BEM-FEM framework in the present study offers an alternative numerical tool for assessing the local fracture response of cracked seawalls.

The objectives of the present study are to: (i) characterize the deformation and stress response of the uncracked seawall and determine the local stress state at the assumed seaward crack location; (ii) develop a coupled BEM-FEM framework for analyzing a seawall containing a pre-existing edge crack in the MATLAB R2025a environment; (iii) use

the coupled BEM-FEM model as a controlled fracture-mechanics sensitivity framework to quantify the effects of crack length, sea-level rise, erosion-induced backfill/support reduction, and crack-face water pressure on the J-integral-based stress-intensity magnitude (K_J) and normal and tangential crack-face displacement jumps, COD_y and COD_x; (iv) compare the consistency between displacement-based and energy-based fracture measures; and (v) assess fracture demand using K_J/K_{IC} and normalized COD; and (vi) perform independent full-FEM ANSYS analyses for representative seawall cases to provide problem-specific corroboration of the predicted fracture-response trends relative to the coupled BEM-FEM predictions.

1.1. Problem Definition and Modeling Assumptions

Conventional stability assessment of concrete gravity seawalls does not directly quantify the localized fracture response of a pre-existing water-accessible crack. The present study addresses the problem of determining how crack length, crack-face hydrostatic pressure, sea-level rise, and erosion-induced reduction in backfill pressure affect the near-tip and crack-face responses of a pre-existing seaward toe-edge crack. Crack initiation and propagation are not simulated; instead, a series of prescribed crack lengths is analyzed to provide a comparative assessment of concrete fracture response under a coastal environment.

The seawall in the present study is represented by an idealized two-dimensional, unreinforced mass-concrete gravity section derived from the historic Galveston Seawall geometry reported in [1] and shown in Figure 3. The section comprises a vertical backfill face, an inclined seaward face, and a base slab supported by a foundation that is not hydraulically accessible. A unit-width section of a long seawall is analyzed under plane-strain conditions, with out-of-plane deformation neglected. The concrete is assumed to be homogeneous, isotropic, linearly elastic, and subject to small deformations. Accordingly, linear-elastic fracture mechanics (LEFM) is used to evaluate the elastic near-tip response before significant nonlinear cracking or material degradation occurs.

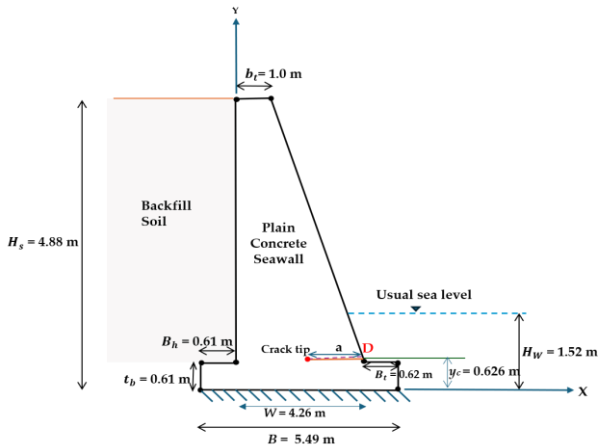


Figure 3. Idealized seawall geometry and local crack-face representation of a two-dimensional plane-strain cross-section, geometric notation, representative seawater level, and location of the pre-existing seaward toe crack at Point (D). The figure is not drawn to scale.

Concrete is treated as a quasi-brittle material, and the limitations of LEFM associated with the fracture process zone are discussed in Section 1. In the present study, LEFM is used only to evaluate the comparative elastic near-tip response of independently prescribed pre-existing cracks. Tensile softening, distributed microcracking, FPZ evolution, and progressive crack propagation are not simulated.

The applied loading on the seawall includes self-weight, active lateral backfill earth pressure, external hydrostatic pressure on the seaward face, and, for the wet-crack cases, hydrostatic pressure acting on the opposing crack faces. Erosion is represented parametrically through prescribed reductions in the backfill contribution. The sea levels used in this study are scenario-based water depths measured from the idealized model base and do not represent NAVD88-referenced site elevations.

The entire base of the seawall is assumed to be fully restrained. Accordingly, the horizontal and vertical displacement components are prescribed as $u_x = u_y = 0$ along the base boundary. This idealized fixed-base condition prevents rigid-body translation and rotation of the seawall and isolates the structural and fracture responses under the applied loading.

The numerical analysis follows two stages. First, an independent ANSYS mechanical model establishes the overall structural behavior and local stress state near the toe region, supporting the assumption that the toe crack is a pre-existing defect rather than a newly initiated crack. Second, the coupled BEM-FEM model developed in MATLAB quantifies the fracture response across the selected crack lengths and coastal scenarios using displacement-based, energy-based and crack-face displacement measures, with numerical reliability assessed through benchmark tests, mesh sensitivity, and domain stability analyses. The published center-cracked-plate problem provides the quantitative benchmark validation of the coupled BEM-FEM formulation, whereas the independent ANSYS seawall analyses provide problem-specific corroboration of the predicted fracture-response trends and relative changes, recognizing that the two models employ different formulations, discretizations, and fracture-parameter evaluation procedures.

1.2. Seawall Parameters and Material Properties

Following the problem definition and idealizations established in Section 1.1, Tables 1 and 2 summarize the geometric and material inputs adopted in the numerical model. Table 1 defines the idealized seawall section, retained-backfill geometry, and crack-reference dimensions, while Table 2 presents the concrete, backfill, and seawater properties used to calculate the structural and fracture responses [14].

Table 1. Geometric parameters of the idealized plain-concrete gravity seawall and pre-existing seaward toe crack.

Parameters	Symbol	Value
Total seawall height	H	4.88 m
Base width	B	5.49 m
Base slab thickness	t_b	0.61 m
Top width	b_t	1.00 m
Heel width	B_h	0.61 m
Toe width	B_t	0.62 m
Reference section width	W	4.26 m
Crack elevation	y_c	0.626 m
Crack mouth offset	-	0.02 m
Retained backfill height above base slab	H_s	4.27 m
Slope		1 V:0.763 H

Table 2. Material, hydraulic, and geotechnical properties of the plain-concrete seawall.

Material Properties	Symbol	Value	Unit
Concrete elastic modulus	E_c	3.0×10^7	kN/m²
Poisson's ratio	ν	0.20	-
Shear modulus	G	1.25×10^7	kN/m²

Unit weight of concrete	γ_c	23.5	kN/m³
Unit weight of seawater	γ_{sw}	10.05	kN/m³
Unit weight of backfill soil	γ_s	18.85	kN/m³
Soil friction angle	ϕ	30	degrees
Rankine active pressure coefficient	K_a	0.333	-
Tensile strength of concrete	f_t	3.0	MPa
Fracture toughness, normal concrete	K_{IC}	0.75	MPa√m
Fracture toughness, aged concrete	$K_{IC,aged}$	0.45	MPa√m
Analysis type	-	Plane strain	-
Out-of-plane thickness	t_h	1.0	m

Unless otherwise specified by a loading scenario, the parameters listed in Tables 1 and 2 remain constant throughout the analysis. The prescribed crack lengths are normalized by the reference width (W = 4.26 m), whereas the water level, crack-face condition, and backfill-reduction factor are varied parametrically. The fracture-toughness values of 0.75 and 0.45 MPa√m represent assumed normal and aged concrete conditions, respectively, and are used only for comparative toughness-normalized screening, not as site-specific measured properties.

1.3. Loading Conditions

This section establishes the loading conditions adopted for the fracture-response analysis. The seawall is subjected to quasi-static self-weight, active lateral backfill earth pressure, external hydrostatic pressure on the submerged seaward surfaces, and, for the wet-crack cases, hydrostatic pressure acting on the opposite crack faces shown in Figure 4. These actions govern the global stress field, crack-face displacement, and near-tip fracture response. Because the adopted BEM formulation is elastostatic, dynamic wave impact, structural inertia, transient fluid-structure interaction, and time-dependent erosion processes are not explicitly simulated in this study.

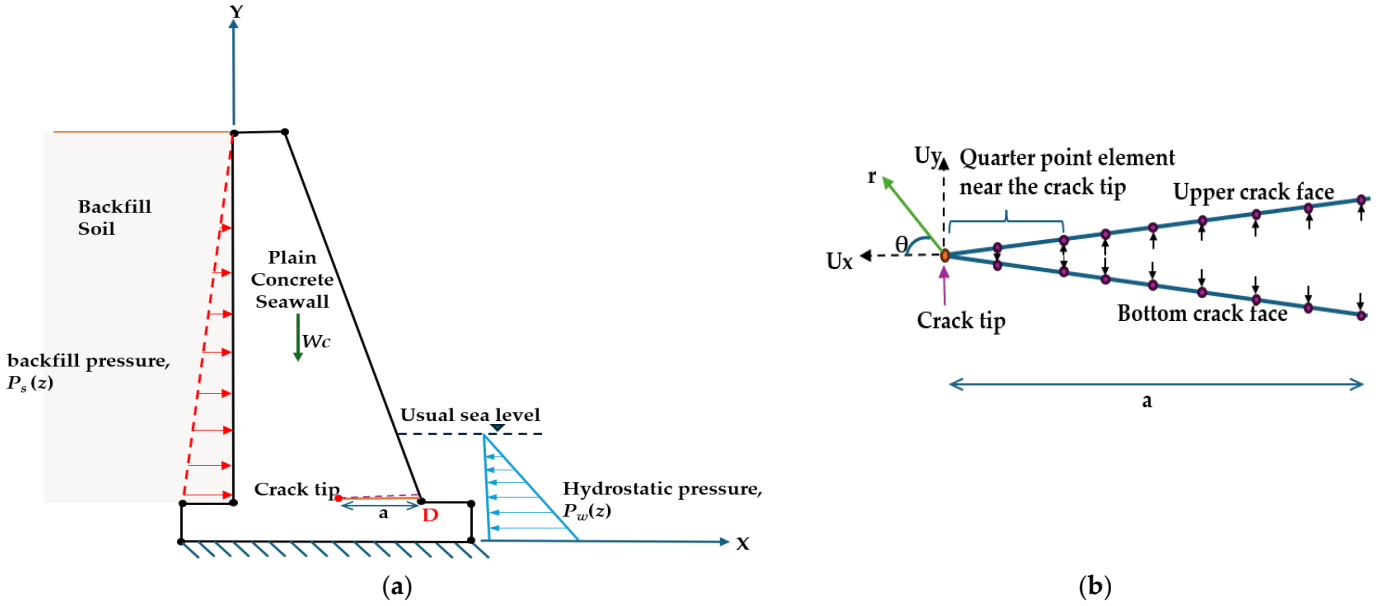


Figure 4. Idealized seawall loading and local crack-face model: (**a**) global geometry showing concrete self-weight, active backfill earth pressure, external hydrostatic pressure, and the pre-existing seaward toe crack; (**b**) magnified crack-face representation showing the local coordinate system, near-tip quarter-point elements, and uniform hydrostatic pressure acting on the opposite crack faces. The figure is not drawn to scale.

Three scenario-based water depths are considered to represent the usual seawater level, a 2050 sea-level-rise condition, and an equivalent extreme coastal seawater level. Case 1 adopts the baseline water depth of (1.52) m. Case 2 incorporates a (0.30) m sea-level-rise increment, giving a water depth of (1.82) m. The adopted 0.30 m increment is consistent with NOAA projections of approximately 0.254–0.304 m of additional sea-level rise along the U.S. coastline by 2050 [6,7]. Case 3 adopts an extreme seawater depth of 3.05 m to represent the combined still-water equivalent of sea-level rise, storm surge, and tidal effects. This extreme seawater level is treated as a hypothetical screening condition to examine the sensitivity of the seawall fracture response to substantially increased hydrostatic demand. These values are prescribed hydrostatic loading scenarios rather than site-specific NAVD88 elevations or simulations of the associated transient coastal processes.

Hydrostatic pressure is applied normally to the submerged seaward boundary and increases linearly with depth below the prescribed still-water level. The external hydrostatic pressure, p_w, is calculated as [2]

$$p_w(y) = \gamma_{sw} (H_w - y),\ y \le H_w \quad (1)$$

where H_w is the seawater level measured from the model-base datum, γ_{sw} is the unit weight of seawater, and y is the elevation of a point on the water-facing boundary.

The active lateral earth pressure on the vertical backfill face is represented using Rankine earth-pressure theory [31,32]

$$p_s(z) = \eta_s \quad K_a \quad \gamma_s \quad z \quad (2)$$

$$K_a = tan^2(45° - \phi/2) \quad (3)$$

where z is the depth below the backfill surface, γ_s is the unit weight of the backfill soil, ϕ is its friction angle, and K_a is the Rankine active earth-pressure coefficient. This simplified formulation assumes cohesionless backfill and neglects wall friction, surcharge, and detailed soil-structure interaction. The dimensionless factor η_s parametrically represents erosion-induced loss of backfill or the backfill-reduction factor. The intact backfill condition is defined by $\eta_s = 1.0$, whereas $\eta_s = 0.75$ and 0.50 correspond to 25% and 50% reductions in backfill earth pressure, respectively. This backfill-reduction factor is not intended to simulate detailed sediment transport or soil-structure interaction.

Because the adopted BEM formulation does not explicitly include a domain body-force term, the concrete self-weight is introduced as a statically equivalent force distribution on the upper boundary of the BEM-FEM interface. For the unit-width plane-strain section, the total concrete self-weight W_c is calculated as

$$W_c = \gamma_c A_s \quad (4)$$

where $A_s = 14.57$ m² is the total cross-sectional area of the entire idealized concrete seawall section per unit out-of-plane width, and γ_c is the unit weight of the seawall concrete. Although the local wall width varies with elevation because of the inclined seaward face shown in Figure 4a, A_s denotes the total integrated area of the complete two-dimensional concrete section and therefore remains constant for the adopted geometry. Equation (4) is used only to determine the total concrete self-weight, W_c.

The resultant acts vertically through the seawall centroid, located at ($x_c = 2.243$) m. Rather than applying the full load at a single node, W_c is distributed among selected BEM-FEM interface nodes on the upper boundary of the local FEM patch. The equivalent self-weight force applied at the interface node (i) is

$$\sum F_{y,i}^{\ self\ weight} = -W_c\, w_i \quad (5)$$

where w_i is the dimensionless nodal distribution weight assigned to the *ith* interface node. Candidate nodes are initially selected within an influence radius $R = 0.80$ m about the wall

centroid and are required to bracket x_c. Gaussian weights are evaluated separately on the left and right sides of the centroid and subsequently normalized so that the discrete nodal forces preserve both the total vertical self-weight and its centroidal moment. The complete node-selection, weighting, normalization, and equilibrium-preservation procedure is provided in Appendix A.

The resulting self-weight contributions are added to the BEM right-hand-side force vector, including the boundary force vector (F_B) and the interface force vector (F_{IB}), as follows:

$$F_B = F_B + F_B^{self\ weight} \tag{6}$$

$$F_{IB} = F_{IB} + F_{IB}^{self\ weight} \tag{7}$$

This equivalent-force treatment represents the global static effect of concrete self-weight without introducing a domain body-force term into the BEM formulation; it does not reproduce the local stress distribution associated with a continuously distributed gravitational body force.

In addition to external hydrostatic loading, the entire crack is assumed to be hydraulically connected to the external seawater in the wet-crack cases. Because the prescribed crack is horizontal and remains at a constant elevation y_c, the hydrostatic head ($H_w - y_c$) is constant along its length. Therefore, a uniform hydrostatic pressure is applied over both crack faces and is given by Equation (8) [11,13].

$$p_c = \gamma_{sw} (H_w - y_c), \quad y_c \le H_w \tag{8}$$

Hydrostatic pressure acting normal to the inclined seaward face includes the corresponding horizontal and vertical force components. For the horizontal wet crack, equal and opposite hydrostatic pressure tractions are applied to the upper and lower crack faces. These tractions act normal to the crack plane and produce a local opening-directed hydraulic action while maintaining zero net vertical resultant over the two crack faces. In the finite element implementation, the uniform crack-face pressure is integrated along the three-node edges of the Q8 elements using one-dimensional Gauss quadrature and converted into consistent nodal forces, $f_{c,e}^{\pm}$, as expressed in Equation (9) [33]:

$$f_{c,e}^{\pm} = \int N_e^T (s)\ t_c^{\pm}\ J_e (s)\ t_h\ ds \tag{9}$$

where N_e contains the quadratic edge shape functions, J_e is the edge Jacobian, and t_h = 1.0 m is the adopted out-of-plane thickness.

Near the crack tip, quarter-point Q8 elements reproduce the LEFM square-root displacement and inverse-square-root stress fields, with the edge Jacobian accounting for the modified geometry [34]. The formulation in the present study assumes a fully water-filled crack with no pressure attenuation, leakage, partial penetration, or transient fluid flow.

1.4. Crack Geometry and Location

A horizontal crack is prescribed near Point D at the water-accessible seaward toe. The independent, uncracked ANSYS Mechanical analysis shown in Section 3.2 indicated local compression at this location under the investigated static loads. Consequently, the crack is not interpreted as having initiated under the current loading scenarios. Instead, it represents a pre-existing defect that may be associated with shrinkage, construction discontinuities, aging, environmental exposure, repeated hydraulic loading, or previous extreme events [2,13]. Its seaward location permits hydraulic connection to external water, enabling explicit evaluation of the influence of crack-face hydrostatic pressure [11,13].

The crack idealized in the present study extends horizontally inward from the seaward face and is represented by upper and lower crack faces terminating at a common tip. This discontinuous representation permits independent crack-face displacements and

the application of equal and opposite water pressure to the two crack faces [35–37]. Quarter-point Q8 elements are used near the crack tip to represent the LEFM singular field.

The prescribed nominal crack length is expressed by a/W, where W = 4.26 m is the reference section width. Seven configurations, a/W = 0.1–0.7, corresponding to physical crack lengths of a = 0.426 m, 0.852 m, 1.278 m, 1.704 m, 2.130 m, 2.556 m, and 2.982 m, are examined to represent short to progressively deeper cracks. Each prescribed crack length is analyzed independently as a separate pre-existing crack configuration and does not represent numerically simulated crack propagation. Accordingly, K_J, K_I^{DET}, and the crack-face displacement measures are interpreted as comparative linear-elastic fracture-response quantities rather than predictions of crack growth. The largest crack ratio, a/W = 0.7, is therefore treated as a sensitivity case within the adopted LEFM framework.

The pre-existing horizontal crack is positioned adjacent to the nominal seaward toe location (D) (see Figure 3) at an elevation (y_c = 0.626) m. Placing the duplicated upper and lower crack-mouth nodes directly on the BEM-FEM coupling boundary would conflict with the continuous displacement representation required at the interface. Therefore, the crack mouth is shifted horizontally by δ = 0.02 m inward from the water-facing boundary so that it lies entirely within the FEM patch. The same offset is used in all cases, and this treatment preserves independent upper- and lower-face displacements while maintaining one-to-one displacement compatibility and force equilibrium at the actual BEM-FEM interface nodes. A crack-mouth offset sensitivity study is additionally performed for Case C-2-b (SLR-Wet) at a/W = 0.1 and 0.5, comparing δ = 0.01 m and 0.02 m. The resulting changes in K_J and $|COD_y|_{max}$ are limited, supporting the use of δ = 0.02 m in the parametric analyses, and the detailed results are provided in Supplementary Table S1.

The loading conditions and crack configurations defined in Sections 1.3 and 1.4 are combined into the parametric analysis matrix summarized in Table 3. Each listed crack length represents a separate coupled BEM-FEM analysis.

Table 3. Parametric coastal loading, backfill-reduction, crack-length, and crack-face conditions adopted in the coupled BEM-FEM fracture analysis of a seawall.

Scenario	Scenario Label	Seawater Level, H_w	Back Fill Sensitivity Factor, η_s	Reduction in Backfill Contribution	Crack Length Ratio, a/W	Crack-Face Condition	Purpose
C-1-a	USL—Dry	1.52 m	1.00	0%	0.1–0.7	Dry	Baseline dry-crack condition
C-1-b	USL—Wet	1.52 m	1.00	0%	0.1–0.7	Wet	Baseline wet-crack condition
C-2-a	SLR—Dry	1.82 m	1.00	0%	0.1–0.7	Dry	SLR dry-crack condition
C-2-b	SLR—Wet	1.82 m	1.00	0%	0.1–0.7	Wet	SLR wet-crack condition without backfill reduction
C-2-c	SLR—Wet—BR 25%	1.82 m	0.75	25%	0.1–0.7	Wet	SLR wet-crack condition with 25% backfill reduction
C-3-a	EXT—Wet	3.05 m	1.00	0%	0.3, 0.5, 0.7	Wet	Extreme wet-crack condition without backfill reduction
C-3-b	EXT—Wet—BR 50%	3.05 m	0.50	50%	0.3, 0.5, 0.7	Wet	Extreme wet-crack condition with 50% backfill reduction
C-3-c	EXT—Wet—BR 25%	3.05 m	0.75	25%	0.3, 0.5, 0.7	Wet	Extreme wet-crack condition with 25% backfill reduction

2. Methodology

The methodology is organized to maintain a consistent mechanical and numerical basis across all comparisons. The seawall representation, coupling procedure, crack-tip treatment, and fracture postprocessing are defined systematically and then applied without modification to the prescribed crack lengths and loading scenarios, as summarized in Figure 5.

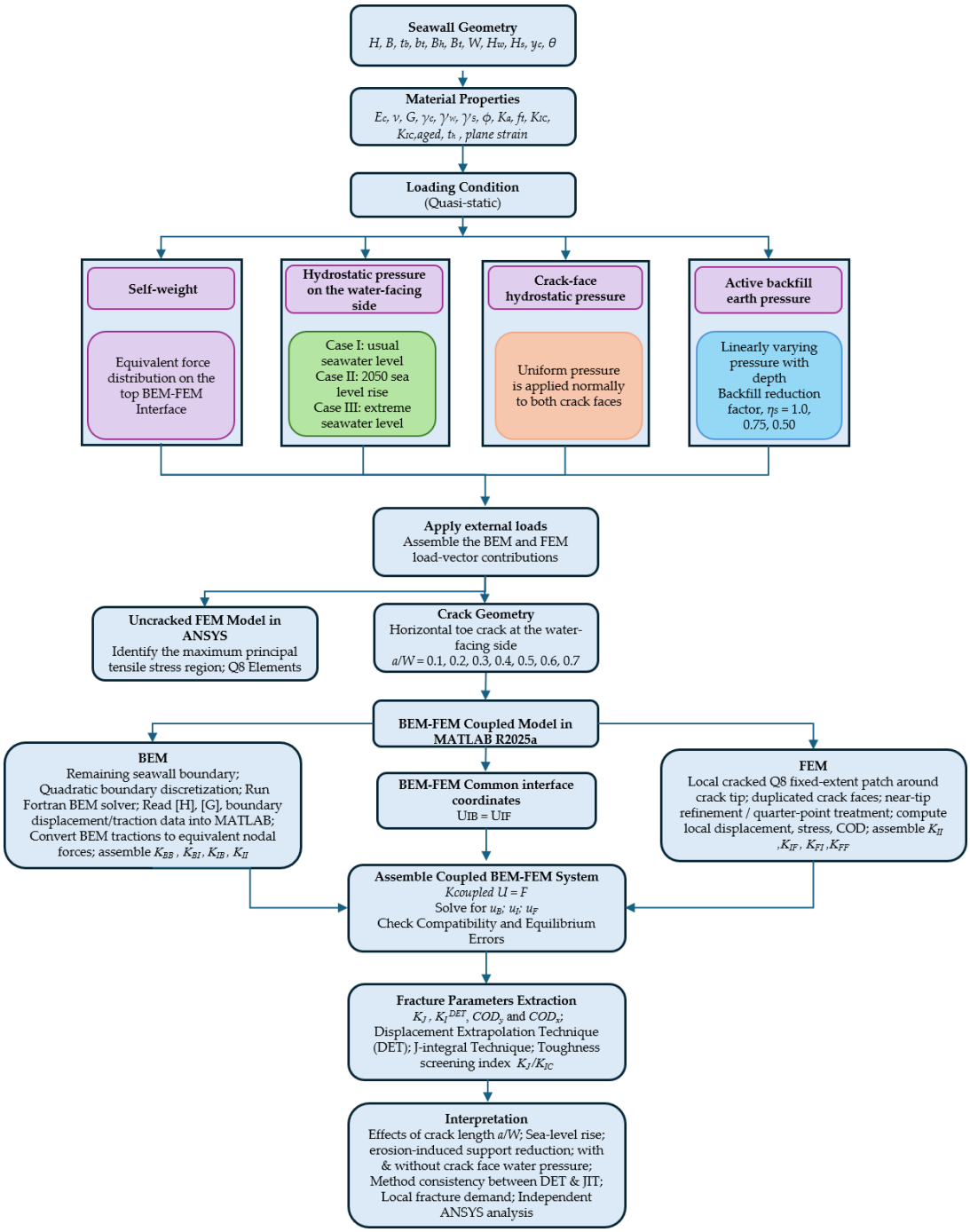


Figure 5. Computational workflow of the MATLAB-based coupled BEM-FEM seawall fracture analysis. The framework incorporates seawall geometry, material properties, four quasi-static loads, and an uncracked FEM model that assesses the local toe stress state, while the prescribed crack is analyzed using a quadratic-element BEM far-field region coupled to a local Q8 FEM patch with duplicated crack faces and quarter-point tip elements. The coupled solution provides K_J, K_J^{DET}, COD_x, COD_y, and K_J/K_{IC} to evaluate the effects of crack length, water level, crack-face pressure, and backfill reduction.

2.1. Coupled BEM-FEM Formulation

2.1.1. Boundary Element Method Formulation

The uncracked far-field portion of the seawall is represented using the two-dimensional direct boundary element formulation for homogeneous, isotropic, linear-elastic plane-strain conditions. The formulation and numerical integration procedures are based on the quadratic-element ELQUABE program presented in [38]. In the direct formulation, the unknown boundary quantities retain their physical meanings as displacements and tractions. In this study, the direct boundary integral formulation is adopted because the boundary unknowns are expressed directly in terms of physical displacements. For a two-dimensional body occupying domain Ω with boundary Γ, the direct elasto-static boundary integral equation can be written as

$$c_{ij}(x)\ u_j(x) + \int_\Gamma H_{ij}(x,s)\ u_j(s)d\Gamma = \int_\Gamma G_{ij}(x,s)\ t_j(s)\ d\Gamma \quad (10)$$

where u_j and t_j are the boundary displacement and traction components, x is the field point, s is the source point on the boundary, G_{ij} and H_{ij} are Kelvin's displacement and traction fundamental solutions, and c_{ij} is the free-term coefficient determined by the local boundary geometry at the source point. The indices i, j = 1, 2 correspond to the two in-plane displacement directions. The fundamental solutions are provided in [24] (p. 2525).

The BEM boundary was discretized using continuous three-node quadratic elements. The element geometry, displacements, and tractions are interpolated isoparametrically as

$$x(\xi) = \Sigma_{k=1}^{3}\ N_k(\xi)x_k \quad (11a)$$

$$u(\xi) = \Sigma_{k=1}^{3}\ N_k(\xi)u_k \quad (11b)$$

$$t(\xi) = \Sigma_{k=1}^{3}\ N_k(\xi)t_k \quad (11c)$$

where ξ is the local element coordinate, varies $-1 \le \xi \le 1$; N_k are the quadratic shape functions. After discretization, the boundary integral equation is assembled into a block matrix expressed as

$$[H]\ \{u\} = [G]\ \{t\} \quad (12)$$

where $[H]$ and $[G]$ are the BEM influence matrices of order $(2N \times 2N)$ matrices where N is the number of boundary nodes. $[G]$ becomes a rectangular matrix of order $2N \times (2N + 2m)$, where m is the number of corners in the geometry, and $\{u\}$ and $\{t\}$ are the prescribed nodal displacement and tractions vectors.

In the present study, the raw $[G]$ matrix, which contains additional corner-traction degrees of freedom from the Fortran solver, is assembled in MATLAB to obtain the square global traction matrix $[G]_{sq}$. MATLAB controls the execution of the Fortran solver, reads the exported matrices and boundary data, and assembles and constructs the required matrices. This MATLAB-Fortran procedure retains the established ELQUABE boundary-integral formulation while extending the original standalone solver to provide a force-compatible BEM operator for direct coupling with the Q8 finite element crack patch.

2.1.2. Finite Element Method Formulation of the Local Cracked Patch

The finite element method is restricted to a fixed-extent local patch surrounding the prescribed seaward toe crack to preserve the same BEM-FEM interface geometry and coupling degrees of freedom. The local patch is discretized using eight-node quadratic isoparametric quadrilateral elements under plane-strain conditions. For each element, the nodal force (f) and displacement vectors (d) are related through the standard finite element equilibrium Equation (13):

$$f = K_e * d \tag{13}$$

where K_e is the element stiffness matrix, which can be formulated in the local coordinates (ξ,η), which vary from −1 to 1 within the element. In terms of global coordinates, K_e is expressed by transforming local coordinates through the Jacobian matrix, as described in [33].

The crack is represented explicitly by duplicated nodes along its upper and lower faces, allowing the two faces to undergo independent normal and tangential displacements. The crack-tip node remains common to both faces, thereby maintaining geometric continuity at the tip. This discretization permits direct evaluation of the crack-face displacement jumps and the application of water pressure to the opposing faces as consistent FEM nodal forces.

Standard Q8 elements are used throughout the local FEM patch, while the elements immediately surrounding the crack tip are converted into quarter-point singular elements. The midside nodes on the edges emanating from the crack tip are shifted to one-quarter of the edge length, enabling the quadratic isoparametric interpolation to reproduce the square-root displacement variation and inverse-square-root stress singularity of the LEFM near-tip field without introducing a separate crack-tip element formulation [36,39-41].

In the present MATLAB implementation, the cracked Q8 mesh, duplicated crack-face degrees of freedom, quarter-point node locations, element stiffness matrices, and applied crack-face nodal forces are assembled within the local FEM patch. The FEM equilibrium equation is written as

$$K_{FEM} \quad u_{FEM} = F_{FEM} \tag{14}$$

where K_{FEM} is the stiffness matrix of the cracked FEM patch, F_{FEM} includes the equivalent nodal forces due to applied loads, and u_{FEM} is the FEM displacement vector. The resulting patch stiffness matrix and load vector are subsequently coupled to the force-compatible BEM representation through their common interface.

2.1.3. Coupled BEM-FEM Formulation in MATLAB

The direct BEM formulation described in Section 2.1.1 and the local cracked FEM formulation described in Section 2.1.2 are combined through a conforming interface (I). The uncracked far-field region is represented by quadratic boundary elements, thereby avoiding domain discretization over most of the seawall. The Q8 finite element discretization is restricted to the local toe region, where separate crack faces, crack-face hydrostatic pressure, quarter-point crack-tip elements, and the recovered stress and displacement fields must be represented explicitly. This decomposition retains the boundary-only efficiency of the BEM while focusing on the finite-element degrees of freedom on the region governing the fracture response. Similar BEM-FEM domain-decomposition approaches have been applied to fracture analysis to obtain detailed crack-tip solutions without discretizing the entire domain [24–27].

The coupled procedure is implemented in MATLAB R2025a. MATLAB executes the modified ELQUABE Fortran solver, reads the pre-boundary-conditions, influence matrices [H] and [G], and assembles the square global traction matrix $[G]_{sq}$. The local Q8 stiffness matrix and FEM load vector are assembled independently in MATLAB for each prescribed crack length and loading scenario. The two subdomains have coincident interface nodes with the same displacement degrees of freedom. Coupling is therefore governed by displacement compatibility and force equilibrium:

$$u_{IB} = u_{IF} = u_I \tag{15}$$

$$F_{IB} + F_{IF} = 0 \tag{16}$$

where the subscripts *B*, *F*, and *I* denote the BEM region, FEM region, and common interface, respectively. These conditions ensure continuous displacement transfer and equilibrium of the interface forces.

The BEM equations are expressed in terms of boundary tractions, whereas the FEM equations use nodal forces. The BEM tractions are converted into consistent nodal forces through the quadratic boundary assembly transformation matrix *M* expressed as Equation (17)

$$M = \int_{\Gamma e} N^T N \, d\Gamma \tag{17}$$

where *N* is the quadratic boundary interpolation matrix, and Γ_e is the element boundary. This transformation provides a force-compatible representation of the BEM boundary for coupling with the FEM system. Using the discrete BEM relation, Equation (12), the equivalent stiffness relation is given by

$$F_{BEM} = [M]\,[G^{-1}]_{sq}[H]\{u\} \tag{18}$$

$$K_{BEM} = M\, G_{sq}^{-1}\, H \tag{19}$$

where K_{BEM} is the resultant equivalent BEM stiffness matrix, which is generally asymmetric. For assembly with the symmetric Q8 FEM stiffness matrix, its symmetric part is adopted as $K_{BEM,sym}$, using the principle of least-squares minimization [24,42]

$$K_{BEM,sym} = 1/2\,[K_{BEM} + K_{BEM}{}^{T}] \tag{20}$$

After partitioning the BEM degrees of freedom into exterior-boundary and interface components and the FEM degrees of freedom into interface and internal components, the coupled system is assembled as

$$[K_{BB}, K_{BI}, 0; K_{IB}, K_{II,BEM} + K_{II,FEM}, K_{IF}; 0, K_{FI}, K_{FF}]_{coupled}\,\{u_B; u_I; u_F\} = \{F_B; F_{I,BEM} + F_{I,FEM}; F_F\} \tag{21}$$

Equivalently, the final system may be written compactly as

$$[K]_{\text{coupled}}\,\{U\} = \{F\} \tag{22}$$

After solving the coupled system, interface displacement compatibility is checked by comparing the BEM and FEM displacements at the common interface using the expressions below:

$$\textit{Compatibility error}, e_{comp} = \| u_{IB} - u_{IF} \| / \| u_{IF} \| \tag{23}$$

$$\textit{Equilibrium error}, e_{eq} = \| F_{IF+} F_{IB} \| / \| F_{IF} \| \tag{24}$$

These residual checks, together with coordinate matching, matrix conditioning, benchmark validation, mesh sensitivity, and J-domain stability, provide numerical verification of the BEM-FEM coupled implementation.

2.2. Fracture Parameter Extraction

After solving the coupled BEM-FEM system, the FEM crack patch fields are used to evaluate the fracture parameters. In this study, the main fracture quantities considered are (i) normal and tangential displacement jump $COD_x(r_i)$, $COD_y(r_i)$; (ii) displacement-extrapolation technique (DET)-based stress-intensity magnitude, K_I^{DET}; (iii) J-integral-based stress-intensity magnitude, K_J; (iv) toughness-normalized fracture-response screening index, I_K; (v) mode dominance ratio (R_{COD}).

2.2.1. Displacement-Extrapolation Technique

The displacement-extrapolation technique (DET) is a direct method for estimating the Mode I stress-intensity factor (K_I) from the near-tip normal displacement jump between corresponding nodes on the opposing crack faces [35]. The stress-intensity magnitude, K_I^{DET}, is evaluated at selected near-tip locations and extrapolated toward the crack tip. In this study, the absolute normal displacement jump COD_y (r_i) is used; therefore, the resulting quantity represents the apparent displacement-extrapolation magnitude.

$$K_I^{DET}(r) = E'/8[|COD_y(r)|\sqrt{(2\pi/r)}] \quad (25)$$

$$COD_y\ (r_i) = 8K_I/E'[\sqrt{(r/2\pi)}] \quad (26)$$

where $E' = E/1 - \nu^2$ (plane strain) and $E' = E$ (plane stress). In this study, the displacement-extrapolation result is used only as a secondary numerical consistency check to validate path-independent J-integral results, given its sensitivity to the near-tip sampling distance, mesh discretization, and mixed-mode contributions [24,43,44].

2.2.2. J-Integral Technique

In this study, the J-integral is evaluated from the displacement, strain, and stress fields recovered within the FEM crack patch after solving the coupled BEM-FEM system. The computational workflow for evaluating the fracture response of the pre-existing seawall toe crack using the J-integral technique is shown in Figure 6.

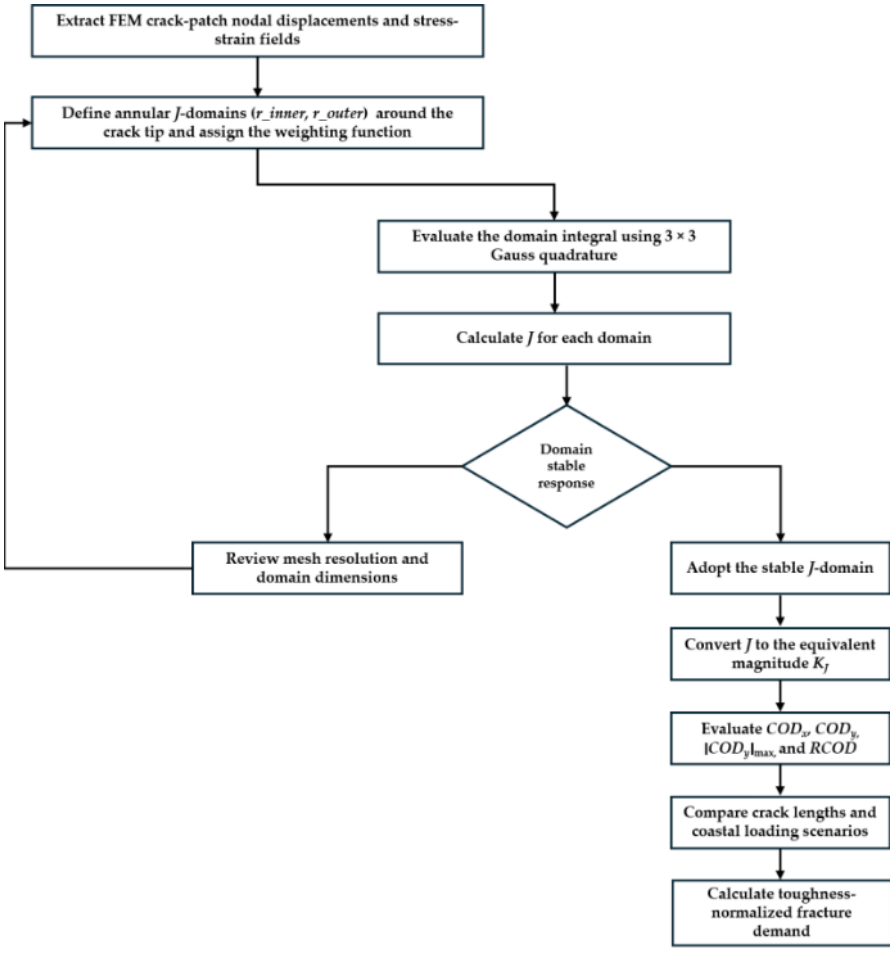


Figure 6. Computational workflow for evaluating the fracture response of the pre-existing seawall toe crack using the *J*-integral technique. The BEM-FEM coupled solution provides the displacement and stress-strain fields within the FEM crack patch. The *J*-integral is then evaluated over multiple

annular domains, checked for domain stability, and converted to the equivalent stress-intensity magnitude K_J. Crack-face displacement measurements and toughness-normalized fracture demand are subsequently calculated to compare crack lengths and coastal-loading scenarios.

For a two-dimensional crack with local crack-extension direction x_1, the contour integral given by [45]

$$J = \int_\Gamma (W_{n1} - \sigma_{ij}\, n_j\, \partial u_i/\partial x_1)\, d\Gamma \quad (27)$$

where the Γ is the contour surrounding the crack tip, n_j is the outward unit normal, and the linear-elastic strain-energy density is given by

$$W = 1/2[\sigma ij\ \varepsilon ij] \quad (28)$$

where σij and εij are the stress and strain fields. In this study, for numerical evaluation, the contour integral is converted into an equivalent domain integral over an annular FEM region, A_J, surrounding the crack, which is given by [45-47]

$$J = \int_{AJ} [\sigma_{ij}\, (\partial u_i/\partial x_1)\, (\partial q/\partial x_j) - W(\partial q/\partial x_1)]\ t\ dA \quad (29)$$

where q is the smooth auxiliary weighting, $q(r) = 1$, if $r \le r_{in}$; $(1 - 3\eta^2 + 2\eta^3)$ if $r_{in} < r < r_{out}$; and 0, if $r \ge r_{out}$; $\eta = (r - r_{in})/(r_{out} - r_{in})$; r_{in} and r_{out} are the inner and outer annular J-domains. The domain integral is evaluated using FEM Q8 elements and 3 × 3 Gauss quadrature; six annular domains are examined, and the J-domain-stable region is identified as 50–250 mm in this study. No symmetry multiplier is applied because both crack faces are modeled in the full FEM patch.

Under plane-strain conditions, the calculated energy-release measure, J is converted to an equivalent stress-intensity magnitude as

$$K_J = \sqrt{(E'|J|)} \quad (30)$$

The raw signed J-integral values were retained and examined for consistency across the selected integration domains before being converted to K_J. Equation (30) uses $|J|$ to define a nonnegative J-integral-based equivalent stress-intensity magnitude. Because the computed crack-face response is closure-directed and crack-face contact is not enforced, K_J is interpreted only as a comparative response magnitude and not as a conventional Mode-I crack-driving stress-intensity factor or deterministic crack-propagation criterion.

2.3. Toughness-Normalized Fracture-Response Screening Index

To compare the calculated fracture demand with the assumed cracking resistance of concrete, the J-integral-based equivalent stress-intensity magnitude is normalized by the Mode-I fracture toughness screening index as

$$I_K = K_J/K_{IC} \quad (31)$$

where I_K is the dimensionless screening index, K_J is the calculated equivalent stress-intensity magnitude, and K_{IC} is the assumed Mode-I fracture toughness. The reference value $K_{IC} = 0.75$ MPa√m and the lower-bound sensitivity value $K_{IC} = 0.45$ MPa√m are considered. Values of ($I_K < 1$), ($I_K = 1$), and ($I_K > 1$) indicate fracture demand below, equal to, and above the adopted toughness, respectively. However, I_K is interpreted only as a comparative screening index because K_J is a non-signed equivalent response magnitude, K_{IC} is a Mode-I material property, and the adopted toughness values are assumed rather than measured for the investigated seawall. The index, therefore, does not constitute a deterministic crack-propagation or failure criterion [48,49].

2.4. Crack-Face Displacement Measures

Crack-face displacements [u_i] are evaluated from the nodal displacement differences between corresponding nodes located on the duplicated upper and lower crack faces ($u_i^{upper} - u_i^{lower}$). For a horizontal crack, COD_y (r_i) represents the normal displacement jump, whereas COD_x (r_i) represents the tangential displacement jump [50]

$$COD_y\ (r_i) = u_{y,i}^{upper} - u_{y,i}^{lower} \tag{32}$$

$$COD_x\ (r_i) = u_{x,i}^{upper} - u_{x,i}^{lower} \tag{33}$$

The radial distance r_i from the crack tip to node pair i is calculated using the average coordinate of the node pair relative to the crack tip location x_{tip}.

$$r_i = [(x_i^{upper} + x_i^{lower})/2] - x_{tip} \tag{34}$$

The normalized relative crack position is expressed as $\varrho_i = r_i/a$, where a is the crack length, $r/a = 0$ corresponds to the crack tip, and $r/a = 1$ denotes the crack mouth.

The principal displacement measures adopted in this study are the maximum normal crack-face displacement-jump magnitude ($|COD_y|_{max}$), separation vs. closure tendency, hydrostatic pressure-induced change ($\Delta COD_{y,p}$ (r_i)), and mode dominance ratio (RCOD). These measures are evaluated over all paired crack-face nodes, and are described below.

Maximum Normal Displacement Jump ($|COD_y|_{max}$): To establish a sign-independent global measure of a normal crack-face deformation over the set of all paired crack-face nodes, N_c, the maximum normal displacement jump is defined as [51].

$$|COD_y|_{max} = \max(i \in N_c)\,|COD_y\ (r_i)| \tag{35}$$

This parameter is evaluated as a global kinematic response measure and is not interpreted as a standardized crack-tip opening displacement (*CTOD*).

Separation vs. Closure tendency*:* Positive COD_y indicates crack-face separation, while negative COD_y indicates a closure tendency under the adopted upper-minus-lower convention. Because crack-face contact is not enforced in this study, negative values indicate that the unconstrained elastic solution tends to close the crack rather than physical interpenetration.

Hydrostatic Pressure-Induced Change ($\Delta COD_{y,p}$ (r_i)): The influence of hydrostatic crack-face pressure is evaluated by comparing identical wet and dry crack configurations. The pressure-induced change between wet and dry cracks in the normal displacement jump is defined as

$$\Delta COD_{y,p}\ (r_i) = COD_y^{wet}\ (r_i) - COD_y^{dry}\ (r_i) \tag{36}$$

A positive $\Delta COD_{y,p}$ means that crack-face water pressure acts in the opening direction or reduces the predicted closure.

Mode Dominance Ratio (R_{COD}): The relative contributions of the normal and tangential displacement jumps are evaluated using the displacement ratio

$$R_{COD}(r_i) = |COD_x(r_i)|/|COD_y(r_i)| \tag{37}$$

Values of $R_{COD} < 1$ indicate that the crack-face displacement response is dominated by the normal component.

2.5. Use of AI-Assisted Tool

During the preparation of this manuscript, the authors used ChatGPT Plus (OpenAI) as an AI-assisted tool to support the organization and interpretation of author-generated numerical results, refinement of technical discussions, and graphical presentation of results. The tool was not used to generate the original numerical simulation results, modify the BEM-FEM computational models, or replace the authors' engineering judgment. All AI-

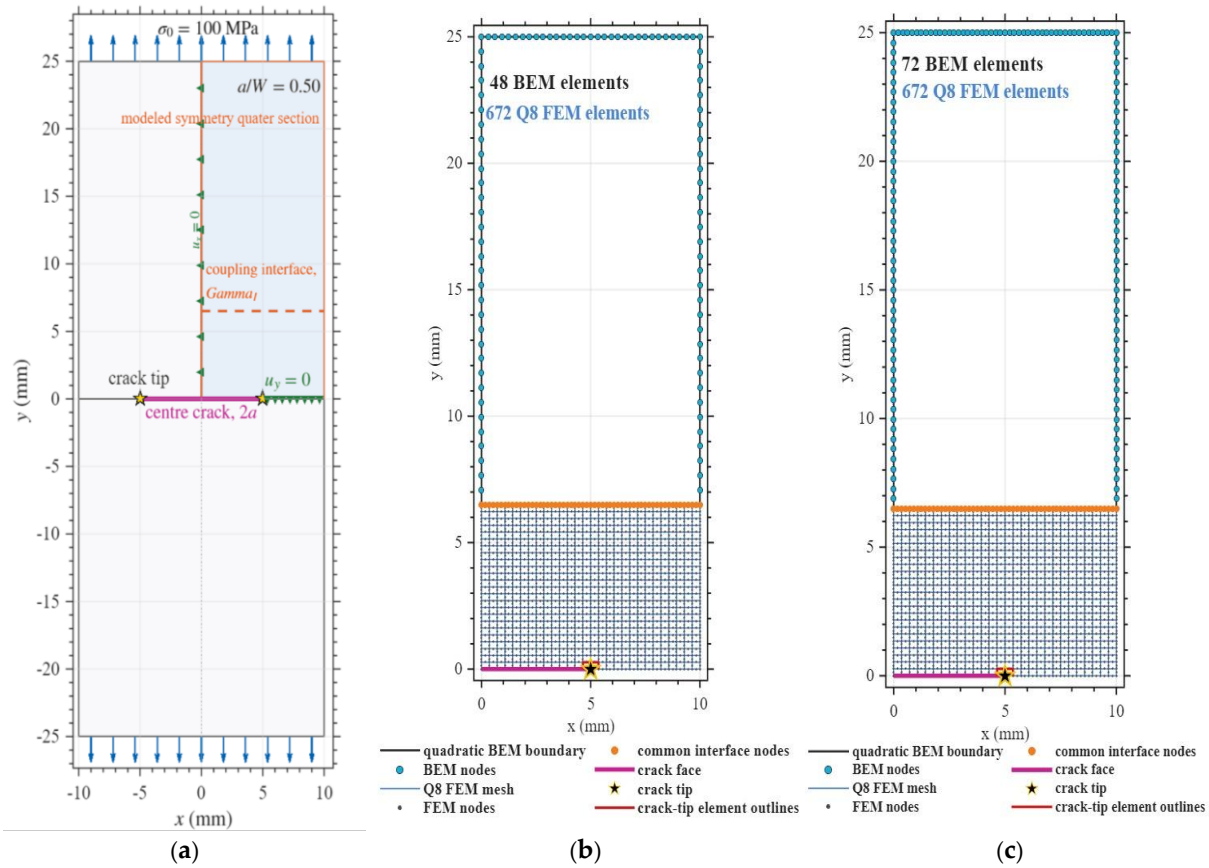
assisted outputs, technical interpretations, and graphical data are independently checked, verified, and revised by the authors, who take full responsibility for the content of the manuscript.

3. Results and Discussions

3.1. Benchmark Validation

To verify the fracture-analysis capability of the coupled BEM-FEM formulation in MATLAB R2025a, the center-cracked finite plate reported by Aour et al. [24] is used as an independent benchmark for this study. The benchmark results are evaluated by comparing the stress-intensity factors obtained from the displacement-extrapolation (K_I^{DET}) and J-integral techniques (K_I) with the analytical Mode-I solution. The effects of BEM-boundary refinement, FEM crack-tip refinement, and J-integral domain selection are examined to assess the accuracy and numerical stability of the coupled formulation.

Figure 7a shows a rectangular plate of width $2W = 20$ mm, height $2H = 50$ mm, and unit thickness containing a horizontal central crack of length $2a$ = 10 mm. The relative crack length is therefore $a/W = 0.5$. The plate is subjected to a uniform tensile stress of $\sigma_0 = 100$ MPa, and the material is homogeneous, isotropic, and linearly elastic, with Young's modulus E = 10,000 MPa and Poisson's ratio $\nu = 0.30$. Taking advantage of geometric and loading symmetry, only the upper-right quarter section of the plate is analyzed. The horizontal displacement is constrained along the vertical symmetry boundary, while the vertical displacement is constrained along the uncracked portion of the horizontal symmetry boundary.

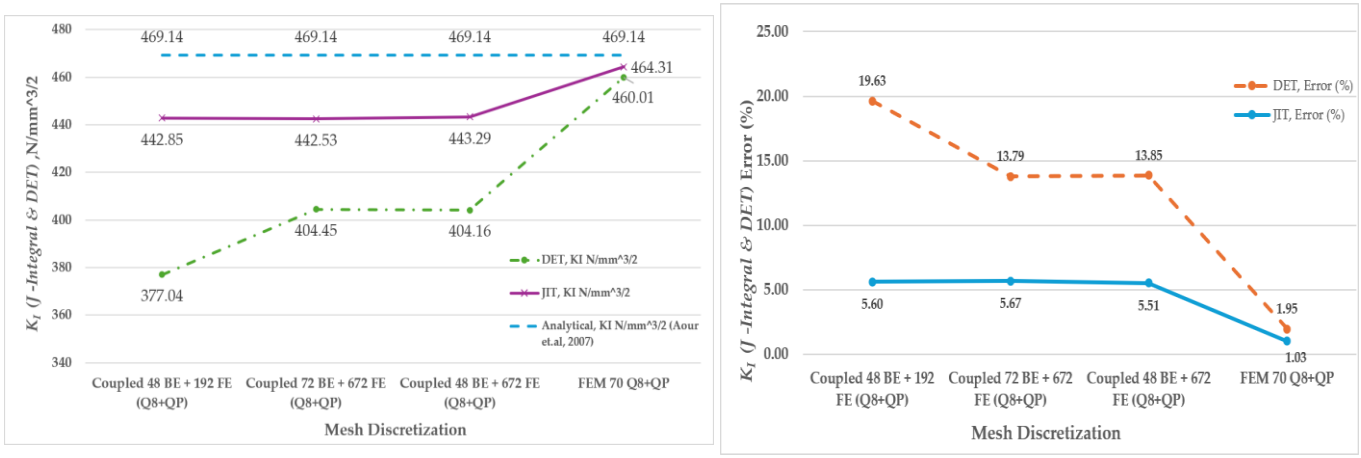


(**a**) (**b**) (**c**)

Figure 7. Geometry, loading, boundary conditions, and numerical discretization of the center-cracked plate: (**a**) full plate and upper-right model-symmetry quarter section; (**b**) coupled discretization comprising 48 quadratic boundary elements and 672 Q8 finite elements; and (**c**) coupled discretization comprising 72 quadratic boundary elements and 672 Q8 finite elements. The FEM region

contains the crack, quarter-point crack-tip elements, and the common BEM-FEM interface. The arrows denote the applied uniform tensile stress, $\sigma_0 = 100$ MPa

Figure 8a shows the benchmark results compared with the analytical value $K_{I,analytical}$ = 469.14 N/mm^(3/2) reported by Aour et al. [24]. For the three coupled discretizations, the J-integral technique produced K_I^J values of 442.85, 442.53, and 443.29 N/mm^(3/2), corresponding to relative differences of 5.60%, 5.67%, and 5.51%, respectively, as shown in Figure 8b. The variation among these coupled J-integral results was less than 0.2%, demonstrating stable fracture-parameter recovery under changes in both the BEM and FEM discretization. The independent full-FEM model produced $K_I^{J}{}_{FEM}$ = 464.31 N/mm^(3/2), with a difference of 1.03%. Whereas the displacement-extrapolation K_I^{DET} results were more dependent on crack-tip refinement, the error decreased from 19.63% to about 1.95%. This difference is expected because displacement extrapolation relies directly on the near-tip nodal displacement field, whereas the J-integral evaluation is energy-based over a finite region surrounding the crack tip and is therefore less sensitive to individual nodal values.



(**a**) (**b**)

Figure 8. Fracture-parameter validation for the center-cracked plate: (**a**) comparison of the Mode-I stress-intensity factors obtained by the displacement-extrapolation technique (DET) and J-integral technique (JIT) with the analytical solution [24]; (**b**) corresponding relative errors for the different coupled BEM-FEM discretization and the independent full-FEM model.

The domain-radius results shown in Figure 9 provide an additional numerical stability check. The computed K_I^J varied by less than 0.5% across the three integration domains for both coupled discretizations, demonstrating satisfactory domain independence over the selected range. The nearly constant coupled results, despite the systematic difference of approximately 5.5–5.7% from the analytical solution, indicate stable interface transfer and fracture-parameter recovery. The remaining difference may reasonably be attributed to the finite coupled discretization, BEM-FEM interface approximation, and numerical evaluation of the crack-tip energy field.

Overall, the benchmark validation supports the capability of the developed formulation to couple the BEM and FEM subdomains, represent the crack-tip singularity using quarter-point elements, and recover a stable J-integral-based stress-intensity magnitude. Accordingly, K_I^J is adopted as the principal fracture-response measure for the subsequent seawall analyses, while the displacement-extrapolation estimate is retained as a supplementary comparison. This behavior is consistent with previous coupled BEM-FEM studies in which the BEM represents the uncracked far-field region and a local FEM domain resolves the crack-tip response [23–26].

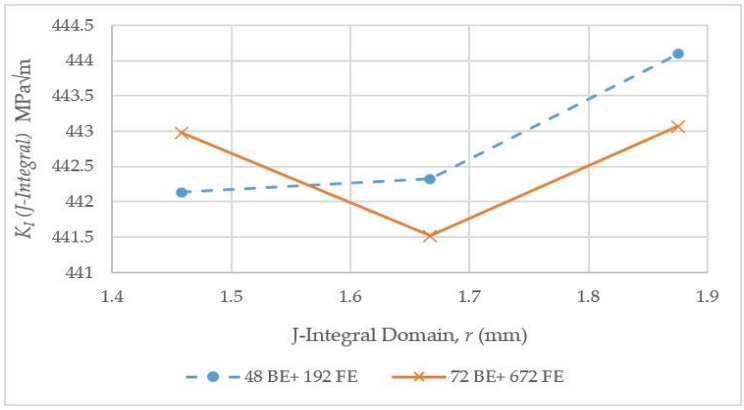
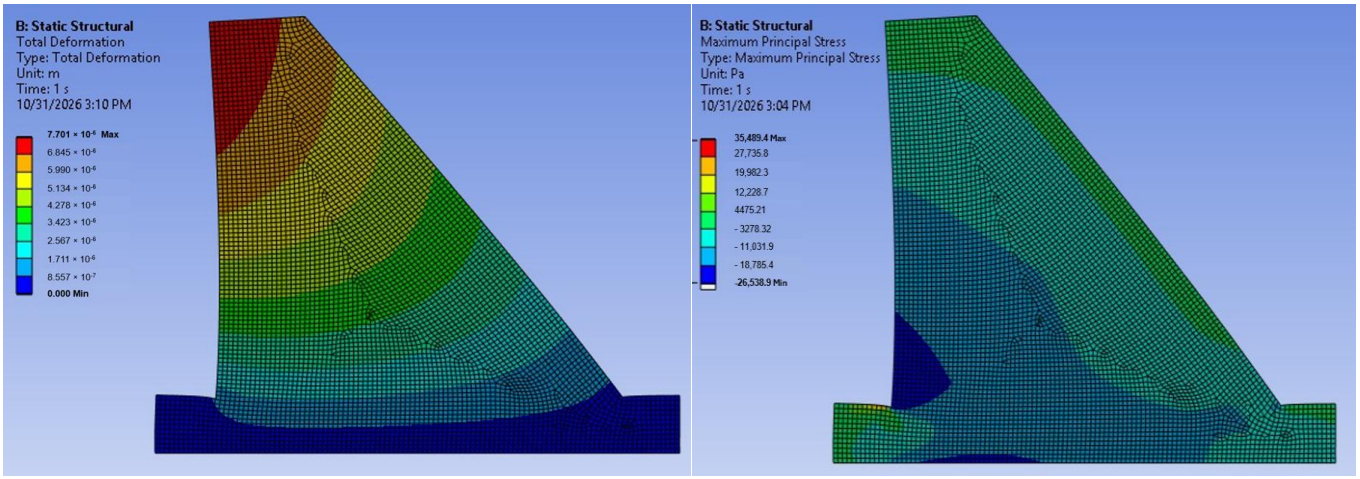


Figure 9. J-integral-based stress-intensity factor, K^I, evaluated using three integration-domain radii for the center-cracked plate. Results are presented for the coupled 48-BE + 192-FE and 72-BE + 672-FE discretization. The limited variation across the integration domains demonstrates satisfactory domain independence and numerical stability of the J-integral evaluation.

3.2. Uncracked Seawall Response and Crack-Location Rationale

Before evaluating the fracture response of the seawall, an uncracked finite element seawall model is subjected to hydrostatic pressure on the seaward side, backfill earth pressure on the soil side, and self-weight. The uncracked seawall is modeled in ANSYS Mechanical 2021R1 under two-dimensional plane-strain conditions using quadratic finite elements. The discretization comprises 5883 elements and 18,002 nodes, with local refinement provided near the seaward toe. The seawall model is analyzed to establish the global deformation and stress state under typical sea-level conditions and to clarify the mechanical basis for the assumed crack location at the toe.

Figure 10 shows the finite element response of the uncracked seawall under the usual sea-level condition H_w = 1.52 m. The model exhibits a maximum total deformation of 0.00770 mm, confirming a small linear-elastic structural response. The global maximum principal stress is 0.0354 MPa, corresponding to only 1.18% of the assumed concrete tensile strength of 3.0 MPa. At the toe, the maximum principal stress is −0.00830 MPa, indicating a locally compressive stress state. Therefore, the applied static loading does not predict initiation of a new Mode-I crack at this prescribed seaward toe location.



(**a**) (**b**)

Figure 10. Uncracked finite element response of the seawall under the usual sea-level condition H_w = 1.52 m with full backfill contribution: (**a**) total deformation; and (**b**) maximum principal stress distribution.

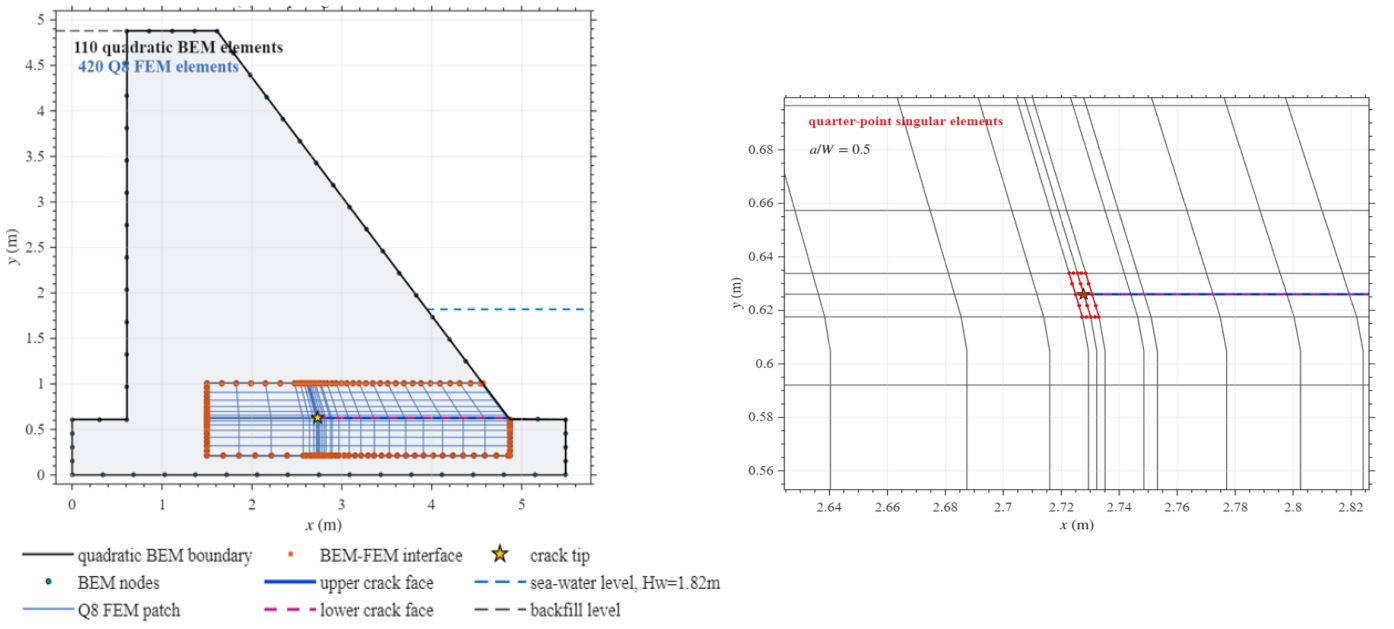
Since Mode-I crack initiation requires a tensile opening field, the calculated compressive toe stress does not support the initiation of a new opening crack under the modeled usual sea-level loading condition [12,15]. The present study focuses on a pre-existing, water-accessible deterioration defect, consistent with cracks and deterioration observed in concrete hydraulic structures [13]. This distinction provides a mechanically consistent basis for investigating the subsequent fracture response of an existing crack subjected to external coastal loading and water-accessible deterioration, with crack-face hydrostatic pressure.

3.3. Discretization Sensitivity Study of Representative Crack Lengths (a/W = 0.5 and 0.7) of Seawall

A combined discretization-sensitivity study is carried out for representative intermediate and long crack lengths of 0.5 and 0.7 under Case C-2-b (SLR-Wet). Table 4 shows three coupled discretizations, M1, M2, and M3, used to assess the combined influence of BEM boundary refinement, FEM crack-tip resolution, coupling-interface discretization, and crack-face sampling on the calculated fracture-intensity measures using displacement-extrapolation stress-intensity factor (K_I^{DET}) and the J-integral-based stress-intensity magnitude (K_J). Figure 11 illustrates the intermediate M2 discretization for a/W = 0.5, including the complete coupled BEM-FEM model and the locally refined crack-tip region containing the quarter-point singular elements.

Table 4. Discretization of the three coupled BEM-FEM meshes used in the mesh-sensitivity study.

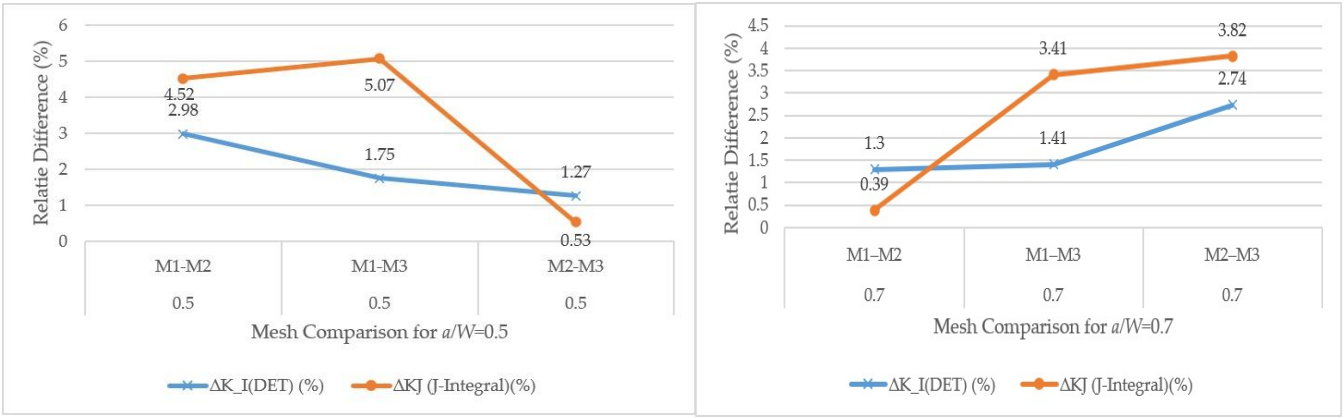
Mesh	BEM Elements	FEM Elements	Interface Nodes	Crack-Face Node Pairs
M1	101	220	117	26
M2	110	420	160	38
M3	120	576	190	48



(**a**) (**b**)

Figure 11. Representative M2 coupled BEM-FEM discretization of seawall for Case C-2-b (SLR-Wet) with a/W = 0.5: (**a**) complete seawall model showing the BEM boundary, local Q8 FEM region, BEM-FEM interface, crack location, and seawater level; (**b**) enlarged crack-tip region showing the locally refined mesh and quarter-point singular elements.

Figure 12 shows limited non-monotonic variations obtained from the three discretizations. Relative differences are calculated with respect to the finer mesh in each comparison pair. For $a/W = 0.5$, the M1-M2, M1-M3, and M2-M3 relative differences were 2.98%, 1.75%, and 1.27%, respectively, for K_I^{DET}, and 4.52%, 5.07%, and 0.53% for K_J. For $a/W = 0.7$, the corresponding differences are 1.30%, 1.41%, and 2.74% for K_I^{DET}, and 0.39%, 3.41%, and 3.82% for K_J. Thus, the maximum variation across the complete mesh range is approximately 5.1%.



(**a**) (**b**)

Figure 12. Mesh-sensitivity assessment of the displacement-extrapolation stress-intensity factor, K_I^{DET}, and J-integral-based stress-intensity magnitude, K_J, for Case C-2-b (SLR-Wet): (**a**) $a/W = 0.5$; and (**b**) $a/W = 0.7$.

The minor non-monotonic behavior is reasonable for the present coupled discretization because refinement simultaneously modifies the BEM boundary representation, FEM crack-tip mesh, interface-node distribution, and crack-face sampling. The results, therefore, demonstrate satisfactory mesh stability rather than strict monotonic convergence. More importantly, the M2-M3 differences remain below 4% for both fracture measures at both representative crack lengths.

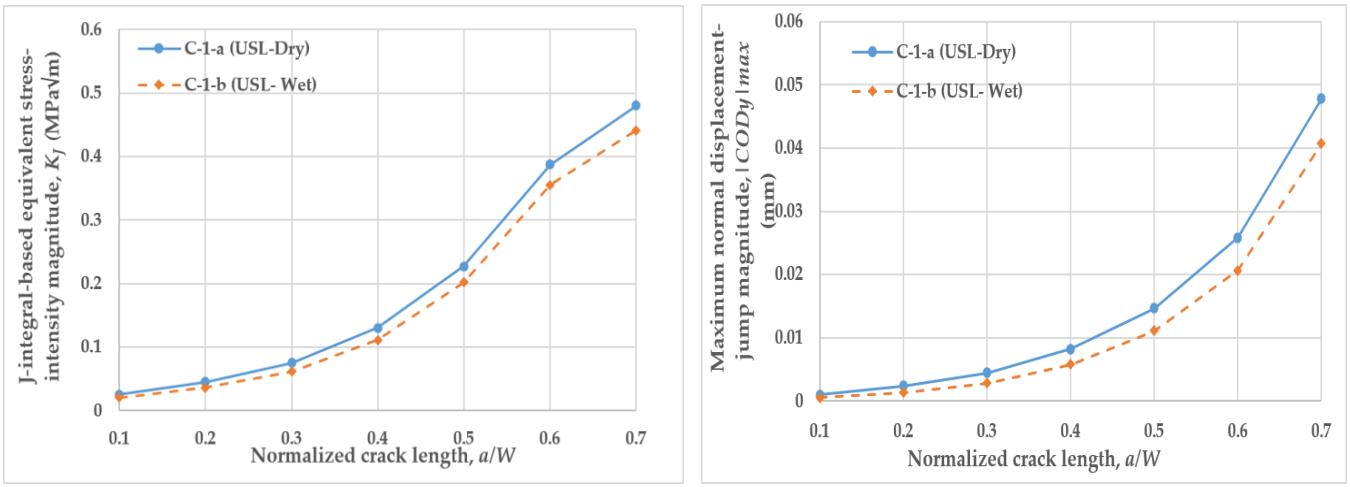
In the present study, Mesh M2 is consequently adopted for parametric analyses across all cases shown in Table 3. Refinement from M2 to M3 increases the number of BEM elements from 110 to 120, the number of Q8 FEM elements from 420 to 576, the number of interface nodes from 160 to 190, and the number of crack-face node pairs from 38 to 48, resulting in only limited changes in K_I^{DET} and K_J. Mesh M2, therefore, provides an appropriate balance between crack-tip resolution, coupling-interface accuracy, and computational efficiency.

3.4. Baseline Fracture Response of a Plain-Concrete Gravity Seawall with Increasing Crack Lengths

The parametric results are presented using controlled matched comparisons derived from Table 3. Within each comparison, one environmental variable is varied while the remaining loading, geometric, material, boundary, and numerical conditions are held constant. This provides a factorial-style, one-variable-at-a-time assessment of crack-face hydrostatic pressure, seawater-level increase, and prescribed backfill-pressure reduction, without attributing the observed response to multiple simultaneously varying parameters.

The fracture response of the seawall under the usual sea-level condition is evaluated for normalized crack lengths ranging from $a/W = 0.1$ to 0.7. Cases C-1-a (USL-Dry) and C-1-b (USL-Wet) are compared to examine the influence of crack-face hydrostatic pressure while maintaining the same seawall geometry, external loading, material properties, backfill contribution, and numerical discretization.

Figure 13a,b show the variation in the J-integral-based equivalent stress-intensity magnitudes, K_J, and maximum normal crack-face displacement-jump magnitudes, $|COD_y|_{max}$, with increasing normalized crack lengths. Both response measures increase nonlinearly with a/W, with a more pronounced increase beyond approximately $a/W = 0.5$. From a/W = 0.1 to 0.7, K_J increases from 0.02 to 0.48 MPa√m for C-1-a (USL-Dry) and reaches approximately 0.44 MPa√m for C-1-b (USL-Wet). Over the same range, $|CODy|_{max}$ increases to approximately 0.047 and 0.041 mm for the dry- and wet-crack conditions, respectively.



(**a**) (**b**)

Figure 13. Baseline fracture response with increasing normalized crack lengths under the usual sea-level condition: (**a**) J-integral-based equivalent stress-intensity magnitudes, K_J; and (**b**) maximum normal crack-face displacement-jump magnitude, $|CODy|_{max}$, for Cases C-1-a (USL-Dry) and C-1-b (USL-Wet).

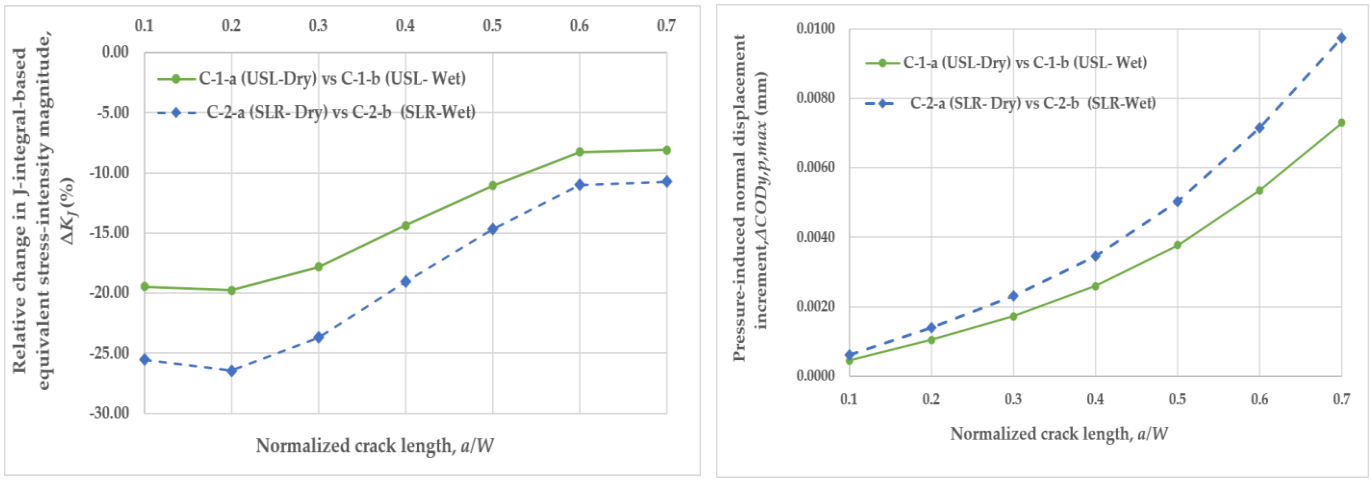
The nonlinear growth of both fracture-response measures is consistent with established fracture-mechanics principles, according to which increasing crack length reduces the intact ligament, increases structural compliance, and intensifies the crack-tip energy response [12,15,28]. The wet-crack case produces lower K_J and $|COD_y|_{max}$ than the dry-crack case. Previous hydraulic-fracture studies have established that internal water pressure exerts opening-directed tractions on accessible crack faces and can promote separation under an opening-dominated loading state [11,16]. In the present seawall, however, COD_y remains negative, and crack-face pressure reduces the tendency toward closure without producing actual opening. This result reflects the superposition and redistribution of crack-face pressure with external hydrostatic, backfill, and self-weight loads. Since crack-face contact is not included, the negative displacement jumps represent a numerical closure tendency rather than physical interpenetration of the crack faces [17].

3.5. Influence of Crack-Face Water Pressure Under Baseline and SLR Conditions

The incremental influence of crack-face water pressure is evaluated through controlled dry-wet comparisons under baseline and SLR conditions. Within each comparison pair, the resulting changes in K_J and COD_y are used to characterize its influence on the near-tip fracture response.

Figure 14a shows that crack-face water pressure reduces the J-derived equivalent stress-intensity magnitude, K_J, relative to the corresponding dry-crack response. The reduction ranges from 8% to 19.46% under the baseline condition and from 10.75% to 25.54% under SLR, with the greatest relative reductions occurring for shorter cracks. However, Figure 14b shows a positive pressure-induced normal displacement increment

$\Delta COD_{y,p,max}$, which increases nonlinearly with crack length, reaching 0.0072 mm under the baseline condition and 0.0097 mm under SLR at $a/W = 0.7$. The larger SLR increments result from the greater crack-face pressure associated with the increased water depth.



(**a**) (**b**)

Figure 14. Influence of crack-face water pressure under baseline and sea-level-rise conditions: (**a**) relative change in the J-integral-based equivalent stress-intensity magnitudes, ΔK_J; and (**b**) maximum pressure-induced normal displacement increment, $\Delta COD_{y,p,max}$, as function of a/W.

The above observed trends are mechanically consistent with the closure-dominated response. Crack-face pressure acts in the opening direction, consistent with previous numerical and experimental studies of water-pressure-driven fracture in concrete [11,16]. In the present analysis, this contribution reduces the negative normal displacement jump, but it does not reverse the total signed COD_y into physical opening. Under linear-elastic superposition, this opening-directed contribution opposes part of the closure-producing field generated by the combined external hydrostatic, backfill, and self-weight loads, thereby reducing the resultant J-integral-based equivalent stress-intensity magnitude. The increasing displacement increment with crack length reflects the greater pressurized crack-face length and structural compliance, whereas the decreasing percentage reduction in K_J reflects more rapid growth of the underlying dry-crack response.

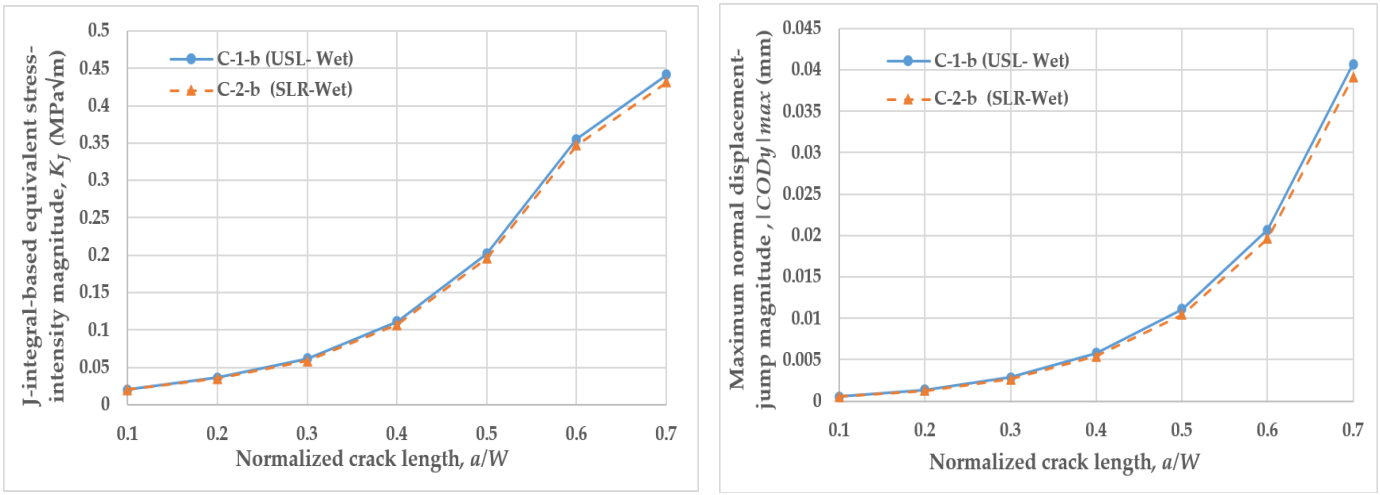
3.6. Effect of Sea-Level Rise on Wet-Crack Fracture Response

The net effect of sea-level rise, from 1.52 m to 1.82 m, under continuously wet crack-face conditions is obtained by directly comparing the baseline cases C-1-b (USL-Wet) and C-2-b (SLR-Wet). Since the crack faces are hydraulically connected to the external water in both scenarios, this comparison isolates the combined influence of the increased external hydrostatic loading and the associated increase in crack-face water pressure.

Figure 15a,b show that both K_J and $|COD_y|_{max}$ increase nonlinearly with a/W for both water levels, with a pronounced increase beyond $a/W = 0.5$. The accelerated response reflects the progressive reduction in the intact ligament and the corresponding increase in structural and crack-face compliance. From $a/W = 0.1$ to 0.7, K_J increases from 0.02 to 0.44 MPa√m for C-1-b (USL-Wet) and from 0.02 to 0.43 MPa√m for C-2-b (SLR-Wet). Similarly, $|COD_y|_{max}$ reaches approximately 0.041 and 0.039 mm, respectively, at $a/W = 0.7$.

Previous studies and engineering guidance recognize that sea-level rise modifies hydrostatic loading, resultant forces, and the stability response of coastal structures [5,9]. The difference between C-1-b (USL-Wet) and C-2-b (SLR-Wet) is attributed to the 0.30 m increase in seawater level and the corresponding increases in external and crack-face hydrostatic pressures. These hydraulic changes modify the lateral resultant, wall rotation, base-stress

redistribution, and near-toe displacement field. The higher seawater level slightly decreases both K_J and $|COD_y|_{max}$. However, the small separation between the curves indicates that sea-level rise has a secondary net influence under the evaluated conditions, whereas crack-length-dependent loss of ligament stiffness remains the primary factor.



(**a**) (**b**)

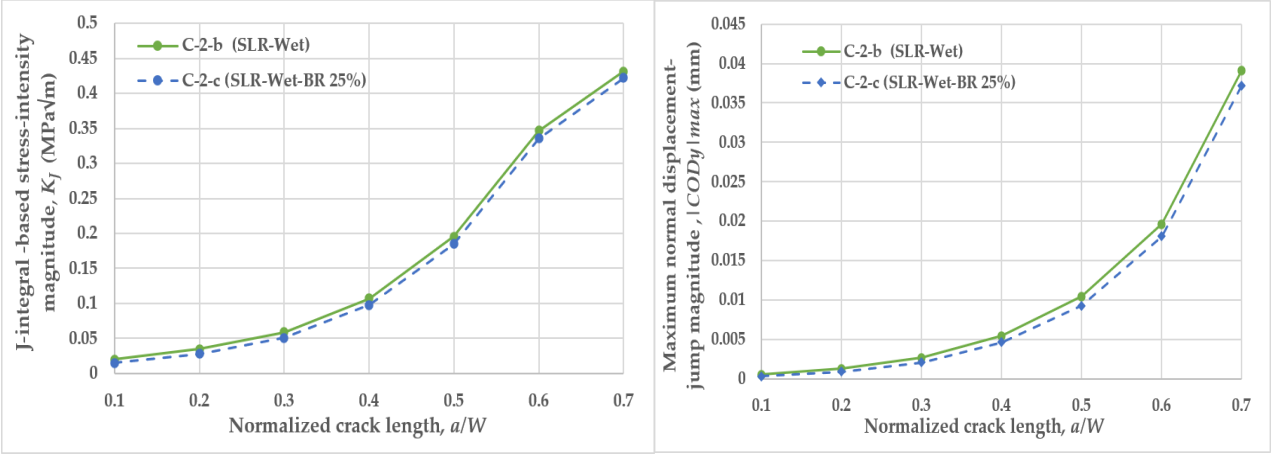
Figure 15. Effect of sea-level rise on the wet-crack fracture response: (**a**) J-integral-based equivalent stress-intensity magnitude, K_J; and (**b**) maximum normal crack-face displacement-jump magnitude, $|COD_y|_{max}$, as a function of a/W, for C-1-b (USL-Wet) H_w = 1.52 m, and for C-2-b (SLR-Wet) H_w = 1.82 m.

3.7. Combined Influence of Sea-Level Rise, Extreme Seawater Level, and Reduced Backfill Support

(a) Influence of Backfill Reduction under SLR Condition

The influence of reduced backfill loading is isolated by comparing C-2-b (SLR-Wet) with C-2-c (SLR-Wet-BR 25%). Both cases maintain the same SLR water level and wet crack-face condition; only the applied backfill-pressure contribution is reduced by 25%.

Figure 16a,b show that both K_J and $|COD_y|_{max}$ increase nonlinearly with a/W, particularly beyond a/W = 0.5, reflecting the reduced intact ligament and increased crack compliance. From a/W = 0.1 to 0.7, K_J increases from 0.02 to 0.43 MPa√m for C-2-b (SLR-Wet) and from 0.015 to 0.42 MPa√m for C-2-c (SLR-Wet-BR 25%). Over the same range, $|COD_y|_{max}$ increases to 0.039 and 0.037 mm, respectively. The reduced-backfill case remains consistently below the full-backfill case, although both follow nearly identical trends.



(**a**) (**b**)

Figure 16. Influence of a 25% reduction in backfill-pressure contribution under the SLR wet-crack condition: (**a**) J-integral-based equivalent stress-intensity magnitudes, K_J; and (**b**) maximum normal crack-face displacement-jump magnitude, $|COD_y|_{max}$, as a function of a/W, for C-2-b (SLR-Wet) and C-2-c (SLR-Wet-BR 25%).

Backfill material outflow can alter the retained material condition behind a coastal structure [21], while active backfill pressure contributes to the lateral resultant and overturning moment acting on the wall [32]. In the present parametric model, only the applied active backfill-pressure contribution is reduced; the wall geometry, water level, crack-face pressure, material properties, and foundation restraints remain unchanged. Backfill pressure contributes to the lateral resultant and overturning moment, thereby influencing wall rotation, base-stress redistribution, and the near-toe displacement field. Backfill reduction slightly decreases both fracture-response measures, K_J and $|COD_y|_{max}$. However, the small separation between the curves indicates that reduced backfill contribution has a secondary influence, whereas crack-length-dependent loss of ligament stiffness remains the primary factor.

(b) Combined Influence of Extreme Seawater Level and Backfill Reduction

The combined environmental condition is evaluated in two stages: First, C-2-b (SLR-Wet, H_w = 1.82 m) is compared with C-3-a (EXT-Wet, H_w = 3.05 m) to evaluate the net effect of increasing the water level under hydraulically connected wet-crack conditions. The influences of 25% and 50% backfill reductions are evaluated under the same extreme water-level condition.

Figure 17a,b show that K_J and $|COD_y|_{max}$ increase nonlinearly with a/W, reflecting the reduction in the intact ligament and the corresponding increase in crack compliance. From a/W = 0.3, 0.5, and 0.7, K_J increases from 0.06 to 0.43 MPa√m for C-2-b and from 0.047 to 0.39 MPa√m for C-3-a. Over the same range, $|COD_y|_{max}$ increases from 0.002 to 0.039 mm and from 0.002 to 0.033 mm, respectively. Increasing the seawater level to 3.05 m reduces K_J by approximately 8–25% and $|COD_y|_{max}$ by 13–45% relative to the SLR condition.

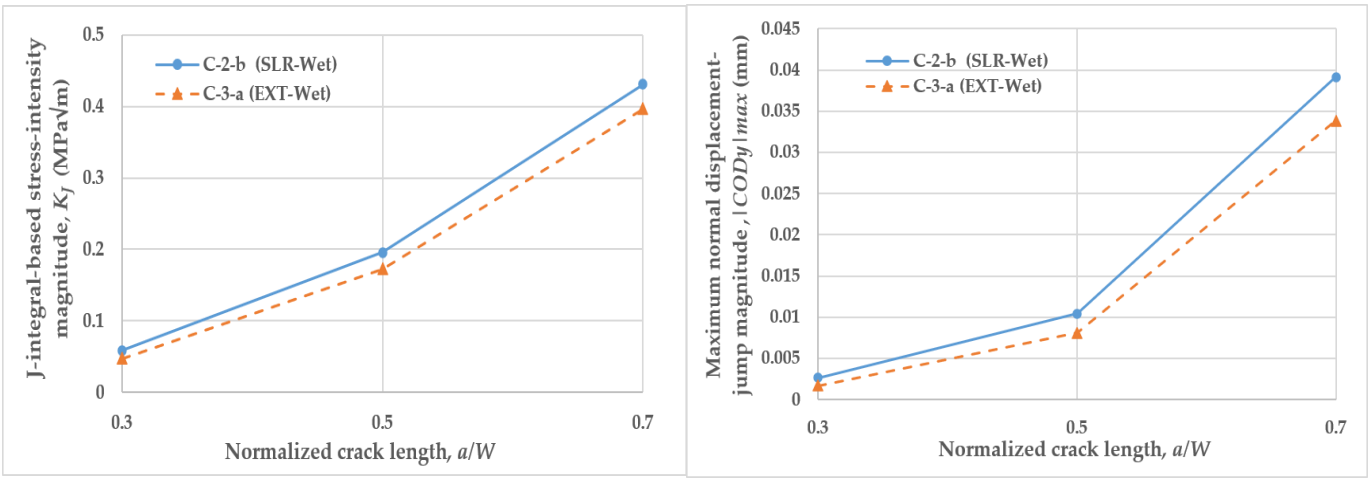
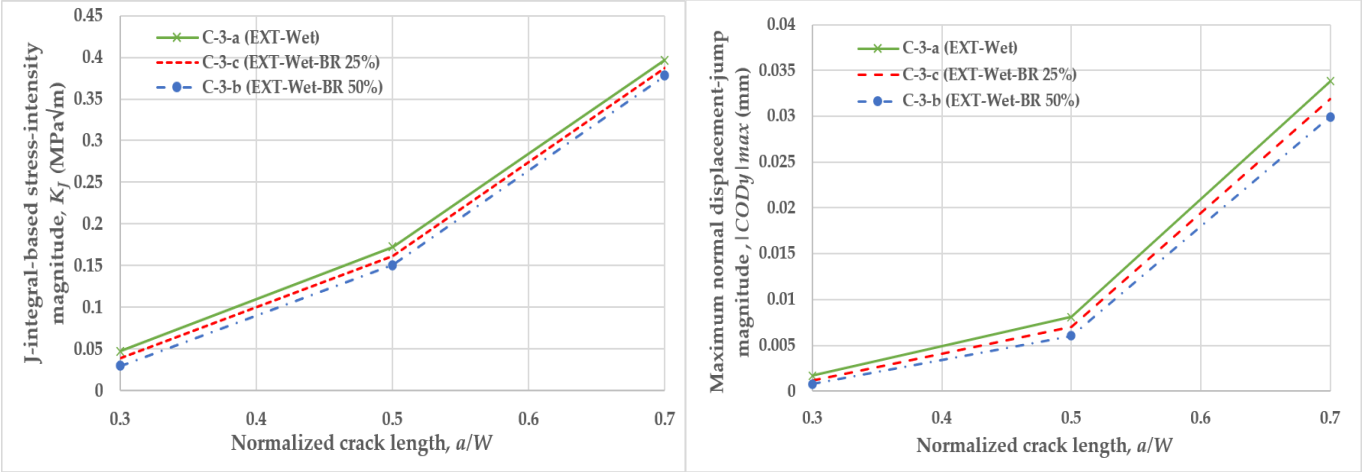


Figure 17. Influence of the extreme seawater level on the wet-crack fracture response: (**a**) J-integral-based equivalent stress-intensity magnitudes, K_J; and (**b**) maximum normal crack-face displacement-jump magnitude, $|COD_y|_{max}$ as a function of a/W, for C-2-b (SLR-Wet, H_w = 1.82 m) and C-3-a (EXT-Wet, H_w = 3.05 m).

The increased seawater level simultaneously modifies the external hydrostatic forces acting on the structure and the pressure acting on the accessible crack faces. The observed trends represent the net redistribution produced by these two hydraulic changes within the existing closure-directed field. Because the external and crack-face pressures vary simultaneously, their individual contributions cannot be separated in this comparison. The results suggest that the combined hydraulic redistribution offsets part of the baseline fracture response, but they do not establish that the external hydrostatic contribution is independently greater than the crack-face-pressure contribution. The relative difference decreases with increasing a/W, supporting the working hypothesis that crack-length-dependent ligament reduction and compliance become increasingly dominant.

In the present model, increasing the prescribed backfill-pressure reduction from 0% to 50% progressively decreases the applied lateral load while the extreme water level, crack-face pressure, geometry, material properties, and boundary conditions remain unchanged. Figure 18a,b show that K_J and $|COD_y|_{max}$ increase nonlinearly with a/W, reflecting the reduction in the intact ligament and the corresponding increase in crack compliance. Across a/W = 0.3, 0.5, and 0.7, K_J increases from 0.04 to 0.39 MPa√m for C-3-a (EXT-Wet), from 0.03 to 0.38 MPa√m for C-3-c (EXT-Wet-BR25%), and from 0.03 to 0.38 MPa√m for C-3-b (EXT-Wet-BR 50%). Over the same range, $|COD_y|_{max}$ increases from 0.001 to 0.034 mm, from 0.001 to 0.031 mm, and from 0.001 to 0.031 mm, respectively.



(**a**) (**b**)

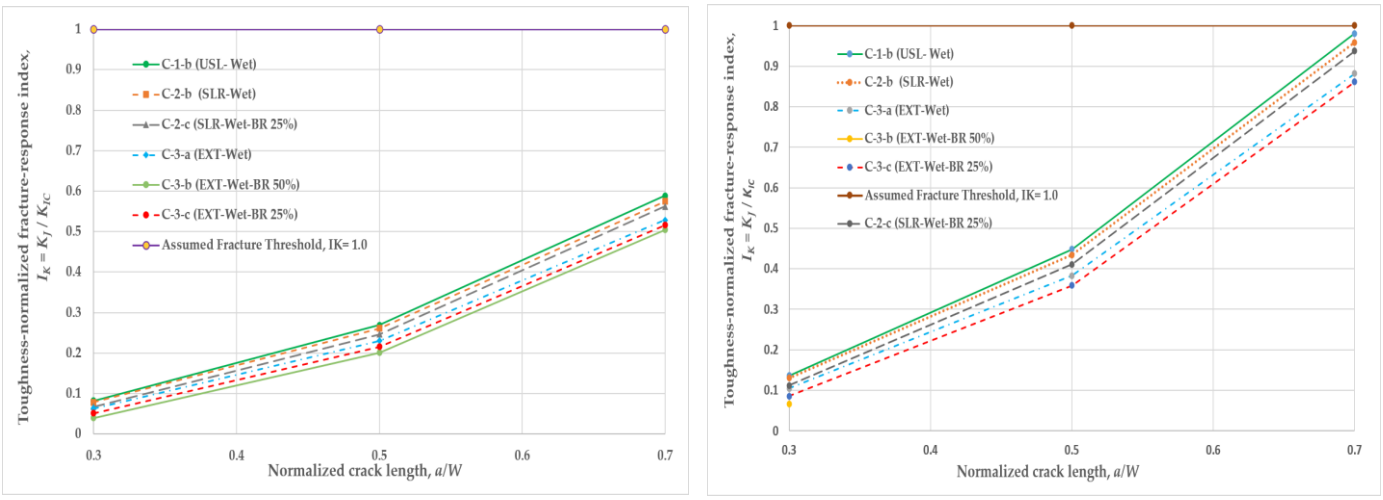
Figure 18. Fracture response under extreme seawater level with varying active backfill-pressure contributions for C-3-a (EXT-Wet), C-3-c (EXT-Wet-BR 25%), and C-3-b (EXT-Wet-BR 50%): (**a**) J-integral-based equivalent stress-intensity magnitudes, K_J; and (**b**) maximum normal crack-face displacement-jump magnitudes, $|COD_y|_{max}$, as a function of a/W.

Relative to C-3-a (EXT-Wet), the 25% and 50% backfill reductions produce progressively lower fracture-response magnitudes, with the relative influence being more pronounced for shorter cracks. This trend indicates that reducing the active backfill pressure reduces the lateral action that contributes to seawall rotation and toe-crack deformation, whereas the effect of crack-length-induced compliance becomes dominant as a/W increases.

3.8. Toughness-Normalized Fracture Response in a Seawall Under Selected Scenarios, I_K

Concrete fracture toughness, K_{IC}, represents the material's resistance to crack extension and provides the critical resistance against which the applied Mode-I stress intensity is compared within linear-elastic fracture mechanics; accordingly, measured K_{IC} values have been used as material inputs in concrete crack-propagation criteria [12,15,52,53]. The computed K_J values are normalized by the assumed concrete fracture toughness, K_{IC}, to assess the relative proximity of the selected coastal responses to a common fracture-mechanics screening limit. Two assumed toughness values, K_{IC} = 0.75 and 0.45 MPa√m, are considered to evaluate the sensitivity of the screening index to concrete fracture resistance.

Figure 19a,b show that the toughness-normalized index $I_K = K_J/K_{IC}$ increases nonlinearly with a/W under all selected scenarios. For K_{IC} = 0.75 MPa√m, I_K increases from 0.04–0.08 at a/W = 0.3 to 0.50–0.59 at a/W = 0.7. When the lower toughness of 0.45 MPa√m is assumed, the corresponding index increases from 0.07–0.14 to 0.84–0.98. The rapid increase between a/W = 0.5 and 0.7 reflects the greater crack compliance and near-tip energy concentration associated with the reduced intact ligament. The scenario-to-scenario differences remain smaller than the influence of crack length and assumed toughness, indicating that these two parameters govern the normalized response.



(**a**) (**b**)

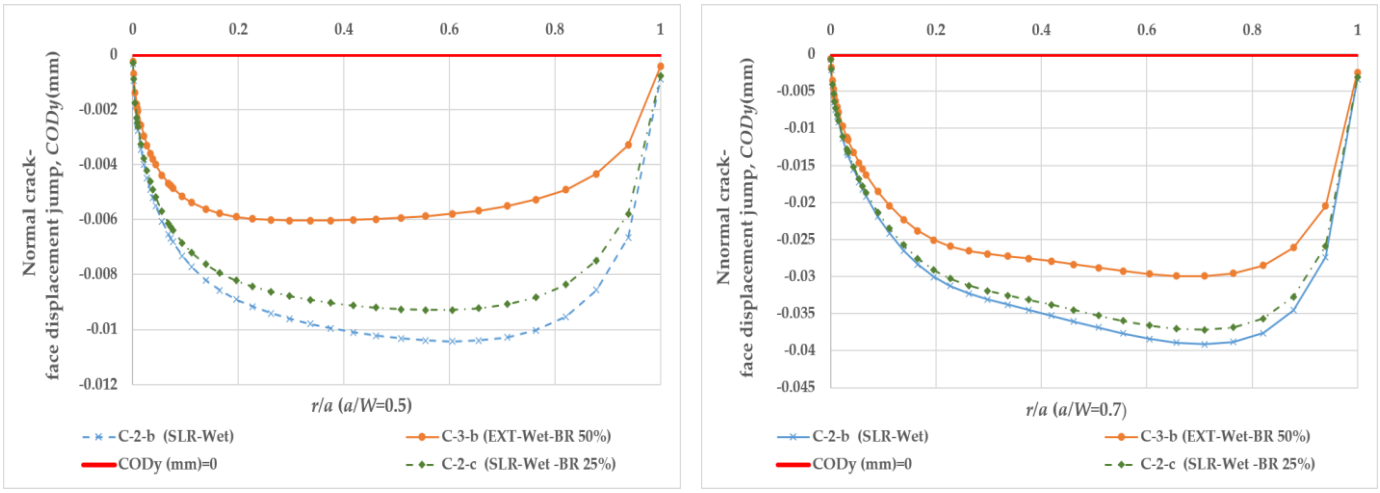
Figure 19. Toughness-normalized fracture-response screening index, $I_K = K_J/K_{IC}$, under selected scenarios for assumed concrete fracture toughness values of: (**a**) K_{IC} = 0.75 MPa√m; and (**b**) K_{IC} = 0.45 MPa√m, as a function of a/W. The horizontal line I_K = 1.0 represents the normalized fracture-response screening limit.

All the computed indices remain below the normalized screening limit of I_K = 1.0. However, the longest cracks approach this limit when the lower toughness is adopted, demonstrating the assessment's sensitivity to the assumed material resistance. Because K_J is an equivalent magnitude and the signed crack-face displacement remains closure-directed, I_K should be interpreted as a toughness-normalized screening index rather than a definitive crack-propagation or failure criterion.

3.9. Crack-Face Displacement Characteristics for Selected Cases of a Seawall

The signed normal crack-face displacement jump is evaluated along the normalized crack coordinate to determine the direction, magnitude, and spatial distribution of relative crack-face movement under specific scenarios. The closure-directed response is mechanically consistent with established fracture mechanics: internal water pressure applies opening-directed tractions to the crack faces [11], whereas a sufficiently strong compressive displacement field promotes crack-face approach and potential contact [17].

Figure 20a,b show that $COD_y(r)$ remains negative for all selected cases and crack-face locations, indicating a closure-dominated response under the adopted sign convention. For a/W = 0.5, the maximum magnitudes of the negative displacement jump are approximately 0.0104, 0.0093, and 0.0060 mm for C-2-b (SLR-Wet), C-2-c (SLR-Wet-BR 25%), and C-3-b (EXT-Wet-BR 50%), respectively. At a/W = 0.7, the corresponding magnitudes increase to 0.039, 0.037, and 0.030 mm. The largest relative approach occurs within the interior crack region, approximately r/a = 0.55–0.70, while the displacement jump decreases toward the crack tip and crack mouth.



(**a**) (**b**)

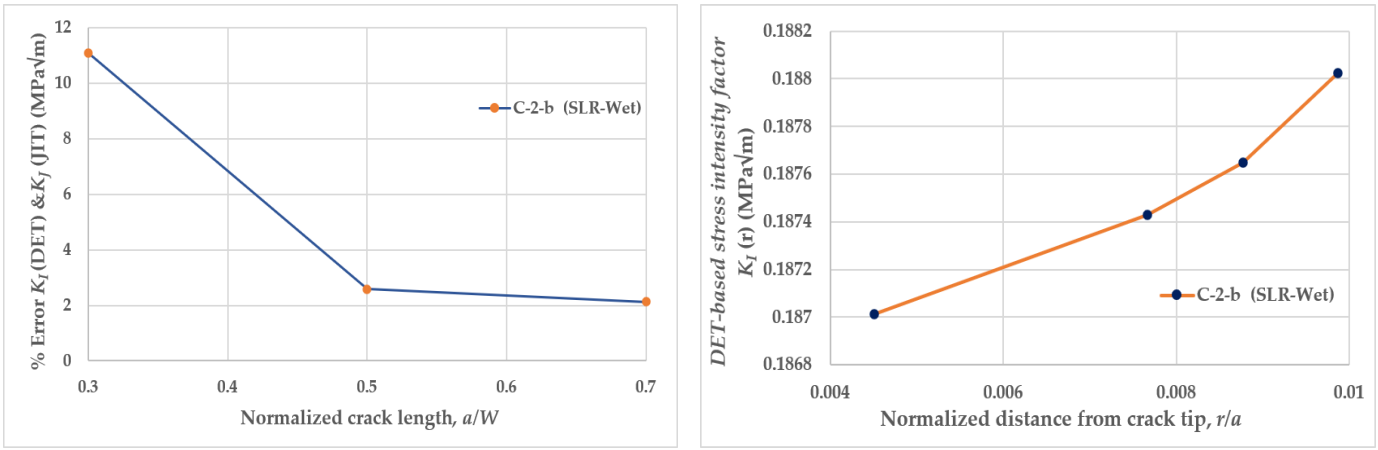
Figure 20. Signed normal crack-face displacement jump, $COD_y(r)$, along the normalized crack coordinate, r/a, for (**a**) a/W = 0.5 and (**b**) a/W = 0.7, under Cases C-2-b (SLR-Wet), C-2-c (SLR-Wet-BR 25%), and C-3-b (EXT-Wet-BR 50%). Negative values indicate relative approach of the crack faces and a closure tendency under the adopted sign convention. The horizontal line at COD_y = 0 distinguishes closure-signed and opening-signed responses.

The substantially greater displacement magnitude at a/W = 0.7 reflects the increase in structural compliance resulting from the longer crack and reduced intact ligament. Relative to C-2-b (SLR-Wet), the reduced closure magnitudes for C-2-c (SLR-Wet-BR 25%) and C-3-b (EXT-Wet-BR 50%) indicate that decreasing the active backfill-pressure contribution reduces the lateral action contributing to seawall rotation and toe-crack deformation. Although C-3-b (EXT-Wet-BR 50%) includes the extreme seawater level, its simultaneous 50% backfill reduction yields the lowest closure magnitude. In the present seawall model, the positive displacement increment produced by crack-face water pressure is insufficient to reverse the negative normal displacement jump generated by the combined self-weight, backfill-pressure, and external hydrostatic loading; thus, the resultant response remains closure-directed under all evaluated scenarios. Because crack-face contact is not included, negative COD_y values represent a numerical closure tendency rather than physical interpenetration.

3.10. Comparison of Displacement Extrapolation (DET) and J-Integral Measures

The apparent DET-based stress-intensity factor, K_I^{DET}(r), is compared with the J-integral-stress-derived magnitude, K_J, to evaluate the consistency of the two fracture measures and the sensitivity of the DET result to the selected near-tip sampling distance.

Figure 21a shows that the absolute relative difference between K_I^{DET} and K_J decreases from 11.10% at a/W = 0.3 to 2.58% and 2.12% at a/W = 0.5 and 0.7, respectively, for Case C-2-b (SLR-Wet). The larger difference for the shorter crack is attributed to its lower fracture-response magnitude and greater sensitivity to local displacement sampling and discretization. For the longer cracks, the close agreement indicates that the near-tip displacement field and contour-based energy measure capture a consistent increase in fracture response.



(**a**) (**b**)

Figure 21. Absolute relative difference between displacement-extrapolation and J-integral fracture measures for Case C-2-b (SLR-Wet): (**a**) absolute relative difference between the DET-based Mode-I stress-intensity estimate, K_I^{DET}, and the J-derived equivalent stress-intensity magnitude, K_J, for a/W = 0.3, 0.5, and 0.7; and (**b**) variation of the apparent DET-based stress-intensity factor, $K_I^{DET}(r)$, with normalized distance from the crack tip, r/a, for a/W = 0.5.

Figure 21b shows that $K_I^{DET}(r)$ varies only from 0.1870 to 0.1880 MPa√m over the selected near-tip interval, corresponding to a variation of less than 0.54%. This limited distance sensitivity supports the stability of the selected DET estimate. The remaining difference is expected because DET is obtained from the local asymptotic displacement field at discrete sampling points, whereas K_J is derived from the energy accumulated over an integration contour. For the normal-component-dominant case response (see section 3.12), the agreement supports using K_J as the primary fracture measure, with K_I^{DET} providing an independent near-tip comparison. These findings are also supported by established literature indicating that K_J provides a stable primary measure of fracture response magnitude, while K_I^{DET} serves as an independent local consistency check [24,43].

3.11. Domain Stability of the J-Integral-Derived Stress-Intensity Magnitude

The sensitivity of the computed K_J to the selected integration contour is examined over six J-integral domains at the representative crack length a/W = 0.5. The inner and outer radii (r_{in} and r_{out}), measured from the crack tip, are defined as D1: (40, 120) mm, D2: (50, 150) mm, D3: (50, 200) mm, D4: (50, 250) mm, D5: (75, 250) mm, and D6: (100, 250) mm. Four wet-crack scenarios are evaluated to verify the stability of the adopted fracture-response measure under different loading conditions.

Figure 22 shows that K_J remains comparatively stable over Domains 1–4 for all evaluated cases. Within this range, the values are 0.20–0.21 MPa√m for C-1-b (USL-Wet), 0.19–0.20 MPa√m for C-2-b (SLR-Wet), 0.18–0.19 MPa√m for C-2-c, and 0.15–0.16 MPa√m for C-3-b (EXT-Wet-BR 50%). The corresponding domain-to-domain variation remains approximately 3–4%, indicating satisfactory contour stability of the near-tip energy measure.

Domains 5 and 6 exhibit modest departures from the stable-domain trends. These deviations may reflect the increasing extent of the integration contours and their greater sensitivity to nonlocal loading regions, geometric boundaries, or the BEM-FEM interface. Therefore, the mean value over Domains 1–4 is adopted as the representative K_J. The consistent stability across the four scenarios supports the numerical reliability of the J-integral evaluation within the selected near-tip domain range.

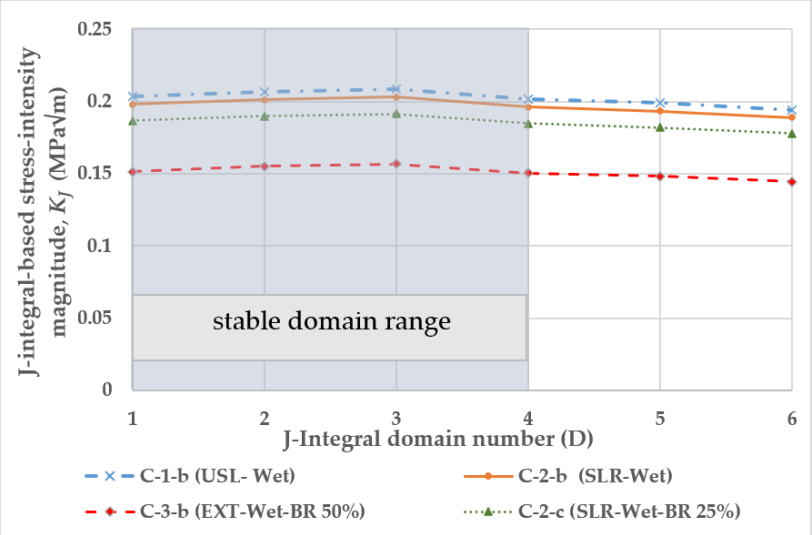


Figure 22. Domain stability of the J-integral-derived equivalent stress-intensity magnitude, K_J, for four representative wet-crack selected scenarios at $a/W = 0.5$. The domain labels D1-D6 correspond to the inner and outer radii specified in Section 3.11.

3.12. Mode Dominance of Crack-Face Displacement Under Selected Scenario

The present study examines the relative normal and tangential crack-face displacement components and compares them at the common near-tip coordinate $r/a = 0.05$ to characterize the dominant displacement mode under selected wet-crack scenarios.

Figure 23 shows that $R_{COD} = |COD_x|/|COD_y|$ falls below unity for each scenario and crack length, which confirms that the normal displacement component exceeds the tangential component. At $a/W = 0.3$, R_{COD} ranges from 0.24 to 0.32 and decreases to 0.22–0.23 at $a/W = 0.5$. At $a/W = 0.7$, the ratio decreases further to 0.054–0.076, indicating that the normal component is approximately 13–18 times greater than the tangential component. The progressive reduction in R_{COD} indicates that the normal displacement jumps increase more rapidly than the tangential displacement as crack length increases. This behavior is consistent with the predominantly normal deformation of the horizontal toe crack under the combined seawall loading. The results support a normal-component-dominant response rather than a purely Mode-I condition because a finite tangential component remains. Furthermore, the negative signed COD_y values indicate that the normal response is closure-directed rather than an actual opening mode [17,20].

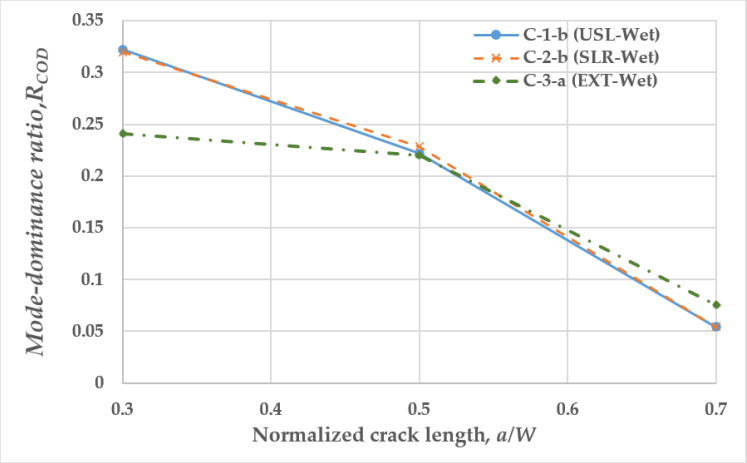


Figure 23. Mode-dominance ratio, $R_{COD} = |COD_x|/|COD_y|$, evaluated at the common normalized crack coordinate $r/a = 0.05$ for Cases C-1-b (USL-Wet), C-2-b (SLR-Wet), and C-3-a (EXT-Wet), as a

function of normalized crack length, a/W. Values below unity indicate dominance of the normal crack-face displacement component over the tangential component.

3.13. An Independent ANSYS Analysis of Plain-Concrete Gravity Seawall

An independent ANSYS 2021R1 finite-element analysis is performed at the representative crack ratio a/W = 0.5 for C-1-b (USL-Wet, H_w = 1.52 m, full backfill) and C-3-b (EXT-Wet-BR 50%), H_w = 3.05 m, 50% backfill reduction) to assess consistency with the coupled BEM-FEM fracture-response predictions. The concrete self-weight, external hydrostatic pressure, backfill earth pressure, and crack-face hydrostatic pressure are represented consistently with the MATLAB formulation, as shown in Figure 24.

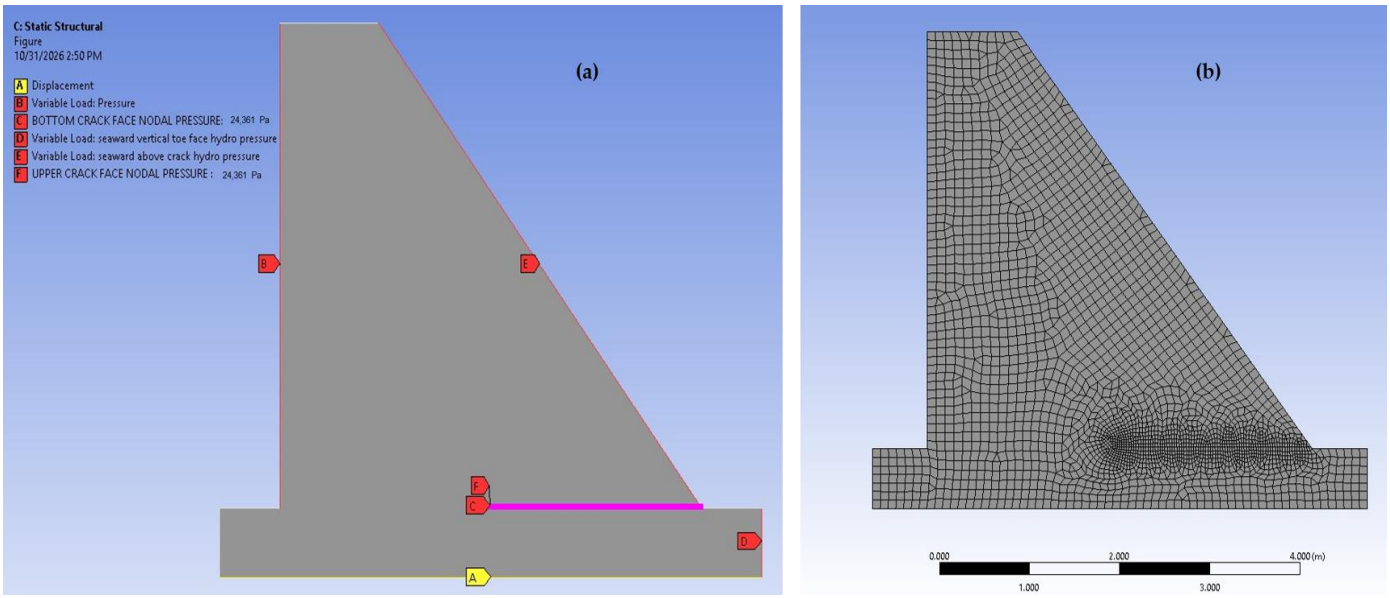
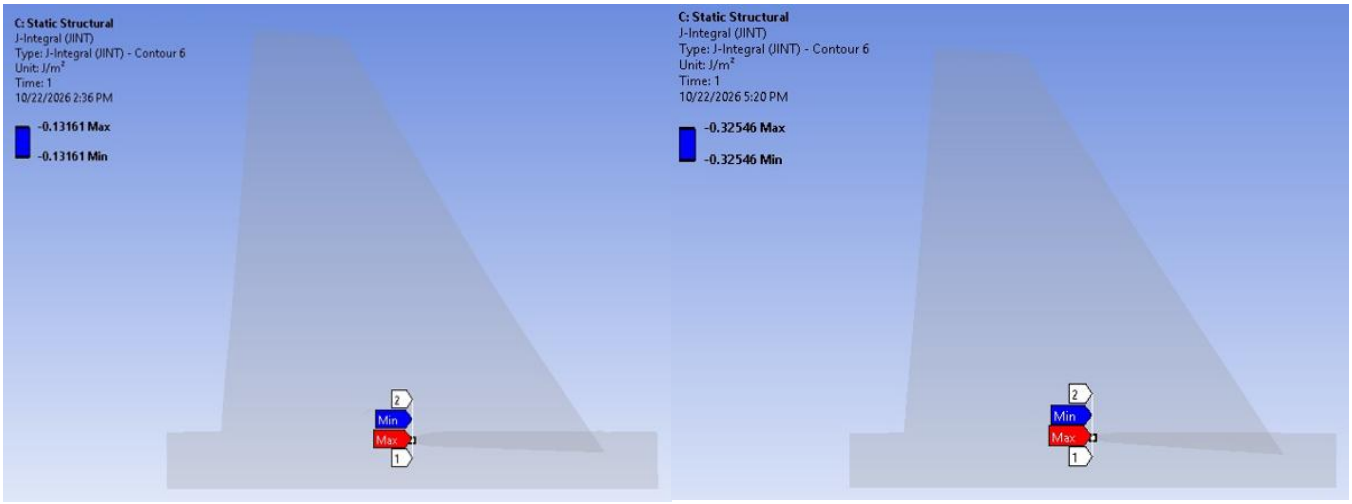


Figure 24. Independent ANSYS model of the cracked plain-concrete gravity seawall at a/W = 0.5: (**a**) geometry, applied loads, and boundary conditions; and (**b**) finite-element mesh with 2633 quadratic elements with local refinement along the crack and near the crack tip.

ANSYS reports the J-integral with a sign determined by the specified crack-extension direction and the contour-orientation convention. Under the crack orientation adopted in the present ANSYS models, the converged contour values were negative for both representative cases. The negative sign is therefore retained when reporting the raw ANSYS output but is not interpreted as a negative fracture-response magnitude. For comparison with the nonnegative MATLAB quantity, K_J, the absolute ANSYS values, $|J|$, are used in Equation (30). This treatment is consistent with Section 2.2.2 and permits comparison of response magnitudes without assigning a physical Mode-I opening interpretation to the raw sign.

The ANSYS J-integral results exhibited satisfactory contour stability. For C-1-b (USL-Wet), Contours 2–6 converged to a raw value of approximately −0.325 J/m², whereas C-3-b (EXT-Wet-BR 50%) converged to approximately −0.1316 J/m². Based on the absolute values, C-3-b therefore produced a 59.6% reduction relative to C-1-b. Using Equation (30), the corresponding ANSYS equivalent stress-intensity magnitudes decrease from approximately 0.101 MPa√m to 0.064 MPa√m, a reduction of 36.4%. Consistently, the coupled BEM-FEM results decrease from 0.202 to 0.151 MPa√m in K_J and from 0.0111 to 0.00604 mm in $|COD_y|_{max}$, corresponding to reductions of approximately 25.4% and 45.5%, respectively. Figure 25 shows the corresponding ANSYS J-integral contour results for the two representative cases.



(**a**) (**b**)

Figure 25. ANSYS J-integral results for the cracked seawall at $a/W = 0.5$: (**a**) C-3-b (EXT-Wet-BR 50%); and (**b**) C-1-b (USL-Wet). The lower J-integral magnitude for C-3-b confirms the reduction in fracture response relative to the baseline condition. The color legend and numerical annotations correspond to the ANSYS J-integral output for each case.

Although the absolute fracture magnitudes differ because of the distinct full-FEM and coupled BEM-FEM formulations, discretization, interface treatment, and fracture post-processing, both approaches predict a reduction in fracture-response magnitude for C-3-b (EXT-Wet-BR 50%) relative to the baseline C-1-b (USL-Wet) condition. The ANSYS crack-face displacement fields also indicate a closure-directed normal response, consistent with the negative COD_y tendency obtained in MATLAB. Accordingly, the ANSYS results provide independent numerical trend-level corroboration of the principal response characteristics of the coupled BEM-FEM results.

4. Conclusions

This study develops a MATLAB-based coupled BEM-FEM framework for evaluating the linear-elastic fracture response of a pre-existing, water-accessible toe crack in a plain-concrete gravity seawall. The quadratic BEM represents the uncracked far-field region, while a locally refined Q8 FEM patch with quarter-point elements resolves the crack-tip response. For the center-cracked-plate benchmark, the coupled *J*-integral results differed from the analytical solution by approximately 5.5–5.7%, while the variation among the evaluated discretizations remained below 0.2%. The seawall mesh study showed M2-M3 differences of less than 4%, supporting the numerical stability of the adopted discretization.

The uncracked seawall exhibits a maximum deformation of 0.00770 mm and a compressive maximum principal stress of −0.00830 MPa at the prescribed toe under the usual sea-level condition. Accordingly, the modeled loading condition does not support initiation of a new Mode-I crack at this location, and the subsequent fracture analyses are interpreted as the response of independently prescribed pre-existing cracks rather than simulated crack propagation. Across the prescribed crack ratios ($a/W = 0.1$–0.7), crack length is the dominant parameter controlling the fracture response. Both K_J and $|COD_y|_{max}$ increase nonlinearly with a/W, particularly beyond $a/W = 0.5$, because of the progressive reduction in the intact ligament and the increase in crack compliance. At $a/W = 0.7$, the usual sea-level dry- and wet-crack cases reach K_J values of approximately 0.48 and 0.44 MPa√m, respectively.

Crack-face hydrostatic pressure produces an opening-directed displacement increment but does not reverse the total response into crack opening. Compared with the corresponding dry-crack cases, it reduces K_I by approximately 8–19.5% under the baseline condition and by 10.8–25.5% under the sea-level rise condition. Because the signed COD_y remains negative, these results indicate a reduction in the calculated closure tendency rather than physical crack opening.

The environmental variables were evaluated through matched comparisons in which one parameter was varied while the remaining loading, geometric, material, boundary, and numerical conditions were maintained. Increasing the water depth from 1.52 to 1.82 m slightly reduces the wet-crack response. At $a/W = 0.7$, K_I decreases from approximately 0.44 to 0.43 MPa√m, while $|COD_y|_{max}$ decreases from 0.041 to 0.039 mm. Increasing the water depth to 3.05 m reduces K_I by approximately 8–25% and $|COD_y|_{max}$ by 13–45% relative to the SLR condition. These changes represent the combined redistribution associated with increased external hydrostatic pressure and increased crack-face pressure and should not be interpreted as the isolated effect of either contribution. Similarly, prescribed reductions in active backfill pressure result in modest decreases in fracture-response measures. Under the extreme water level at $a/W = 0.7$, increasing the backfill reduction from 0% to 50% decreases K_I from approximately 0.40 to 0.38 MPa√m and $|COD_y|_{max}$ from 0.034 to 0.030 mm. Therefore, sea-level rise and backfill reduction have secondary effects compared with crack-length-dependent ligament loss.

The toughness-normalized index remains below unity for all evaluated cases. At $a/W = 0.7$, I_K ranges from 0.50 to 0.59 for $K_{IC} = 0.75$ MPa√m and from 0.84 to 0.98 for $K_{IC} = 0.45$ MPa√m, showing that long cracks may approach the screening limit when lower fracture toughness is assumed. The displacement response is normal-component-dominant but not purely Mode I, with $R_{COD} = 0.054$ to 0.076 at $a/W = 0.7$. Overall, crack length and assumed concrete fracture toughness govern the screened response, while hydraulic loading and backfill reduction modify its magnitude.

Independent ANSYS analyses provided a problem-specific numerical comparison for representative seawall cases at $a/W = 0.5$. The ANSYS equivalent stress-intensity magnitude decreased from approximately 0.101 to 0.064 MPa√m for C-1-b (USL-Wet) and C-3-b (EXT-Wet-BR 50%), while the coupled BEM-FEM K_I results decreased from 0.202 to 0.151 MPa√m. The corresponding coupled $|COD_y|_{max}$ decreased from approximately 0.0111 to 0.00604 mm. Although the absolute magnitudes differ due to variations in formulation, discretization, interface treatment, and fracture post-processing, both approaches predict a lower fracture-response magnitude for C-3-b and a closure-directed normal crack-face response. The ANSYS analyses, therefore, provide independent, problem-specific corroboration, whereas the published center-cracked-plate test provides quantitative validation of the coupled formulation.

5. Limitations and Future Work

This study is limited to a two-dimensional, plane-strain, quasi-static, linear-elastic model with independently prescribed cracks. Accordingly, the prescribed seawater-level and backfill-reduction scenarios are used only as controlled quasi-static loading conditions for evaluating the local fracture response of the pre-existing crack and are not intended to represent a comprehensive coastal performance, erosion, or soil-structure interaction model. The LEFM formulation does not explicitly represent the concrete fracture-process zone, tensile softening, crack-face contact, progressive crack propagation, nonlinear concrete behavior, leakage, wave impact, transient fluid-structure interaction, or time-dependent erosion.

The coupled BEM-FEM framework presented in this study can be extended to incorporate crack-face contact, crack propagation, nonlinear concrete behavior, and transient hydromechanical loading, including wave impact, uplift, and progressive erosion.

Supplementary Materials: The following supporting information can be downloaded at: https://www.mdpi.com/article/10.3390/coasts6040049/s1, Table S1. Crack-Mouth Offset Sensitivity of Fracture-Response Measures for Case C-2-b (SLR-Wet).

Author Contributions: Conceptualization, R.C.R. and M.A.; methodology, R.C.R.; software, R.C.R.; validation, R.C.R.; formal analysis, R.C.R.; investigation, R.C.R.; resources, R.C.R., S.T.G., and M.A.; data curation, R.C.R.; writing—original draft preparation R.C.R.; writing—review and editing, R.C.R., S.T.G. and M.A.; visualization, R.C.R.; supervision, M.A. All authors have read and agreed to the published version of the manuscript.

Funding: This research received no external funding. The authors sincerely and gratefully acknowledge graduate research assistantship support for their academic appointments provided in part through NASA Grant Award No. 80NSSC22M0293 and the NASA Glenn Research Center, particularly the MUREP Aerospace Academy (MAA) Education Program. This support did not directly fund the research presented in this manuscript.

Data Availability Statement: The original contributions presented in this study are included in the article. The numerical data supporting the findings of this study will be made available from the corresponding author upon request.

Acknowledgments: The senior author and the doctoral student (S.T.G.) acknowledge financial support in the form of graduate teaching assistantships from the Dept. of Civil, Environmental and Geomatics Engineering at Florida Atlantic University (FAU), FL, U.S.A. The authors also thank Anindya Deb of the Indian Institute of Science (IISc), India, for providing relevant literature and initial guidance through e-mail/telephone communications and in-person meetings on the boundary element method at FAU. The authors also thank Mark Albert H. Zarco of the UP Institute of Civil Engineering, for sharing materials related to soil-structure interaction and for initial e-mail communication, and J.N. Reddy of Texas A&M Engineering and graduate student Tanmaye Y. Heblekar for providing basic FEM MATLAB files that were subsequently modified and extended for the present study is removed. During the preparation of this manuscript, the authors used ChatGPT Plus (OpenAI) for assistance with text refinement and selected graphical development tasks. The authors reviewed and edited all outputs and took full responsibility for the content of this publication.

Conflicts of Interest: The authors declare no conflicts of interest.

Appendix A. Equivalent Self-Weight Distribution at the BEM-FEM Interface

The adopted BEM formulation does not explicitly include a domain body-force term, the concrete self-weight is represented by statically equivalent vertical nodal forces applied to coincident BEM-FEM interface nodes along the horizontal upper boundary of the local FEM patch at y = 1.010 m. Candidate interface nodes are initially selected within an influence radius R = 0.80 m about the wall centroid x_c = 2.243055 m. The selected node set is required to bracket the centroid; if this condition is not satisfied, the influence radius is increased in 0.20 m increments until the centroid lies within the selected range.

Gaussian weights $w_{i,L}$ and $w_{i,R}$ are evaluated separately on the left and right sides, as follows:

$$w_{i,L} = \exp[-(x_i - x_c)/\sigma)^2] \quad \text{(A1)}$$

$$w_{i,R} = \exp[-(x_i - x_c)/\sigma)^2] \quad \text{(A2)}$$

where $\sigma = R/2$, and the corresponding weighted centroid locations on the left ($\bar{x_L}$) and right sides ($\bar{x_R}$) are

$$\bar{x_L} = \sum_i w_{i,L}\, x_i \quad \text{(A3)}$$

$$\bar{x_R} = \sum_i w_{i,R}\, x_i \quad \text{(A4)}$$

The fractions of the total self-weight assigned to the right and left node groups are determined from

$$f_R = (x_c - \bar{x_L})/(\bar{x_R} - \bar{x_L}) \quad \text{(A5)}$$

$$f_L = 1 - f_R \quad \text{(A6)}$$

The final nodal weights, w_i, define the downward nodal forces as in Equation (5)

$$w_i = f_R\, w_{i,R} \quad when\ x_i \geq x_c \quad \text{(A7)}$$

$$w_i = f_L\, w_{i,L} \quad when\ x_i \leq x_c \quad \text{(A8)}$$

Therefore, the resulting discrete force system is checked to satisfy both the total vertical gravity resultant represented in Equation (5) and its centroidal moment, as follows:

$$\sum_i x_i\, F_{y,i}^{\ self\ weight} = -W_c\, x_c \quad \text{(A9)}$$

Only downward nodal forces are permitted. This equivalent representation reproduces the global static effect of concrete self-weight and is not intended to reproduce the local stress distribution associated with a continuously distributed gravitational body force.

References

1. U.S. Army Corps of Engineers. *Design of Coastal Revetments, Seawalls, and Bulkheads*; EM 1110-2-1614; U.S. Army Corps of Engineers: Washington, DC, USA, 1995.
2. Hosseinzadeh, N.; Ghiasian, M.; Andiroglu, E.; Lamere, J.; Rhode-Barbarigos, L.; Sobczak, J.; Sealey, K.S.; Suraneni, P. Concrete seawalls: A review of load considerations, ecological performance, durability, and recent innovations. *Ecol. Eng.* **2022**, *178*, 106573.
3. U.S. Army Corps of Engineers. *Coastal Engineering Manual, Part V: Shore Protection Projects*; EM 1110-2-1100; U.S. Army Corps of Engineers: Washington, DC, USA, 2006.
4. Federal Emergency Management Agency (FEMA). *Hurricane Ian in Florida: Building Performance Observations, Recommendations, and Technical Guidance*; Mitigation Assessment Team Report, FEMA P-2342; U.S. Department of Homeland Security: Washington, DC, USA, 2023.
5. Nielsen, L.; Salim, A.; Lord, D.; Withycombe, G.; Armstrong, I. Geotechnical aspects of seawall stability with climate change. In Proceedings of the Coasts and Ports Conference, Perth, Australia, 11–13 September 2013.
6. NOAA. U.S. Coastline to See Up to a Foot of Sea Level Rise by 2050. Available online: https://www.noaa.gov/news-release/us-coastline-to-see-up-to-foot-of-sea-level-rise-by-2050 (accessed on 7 July 2026).
7. NOAA Climate.gov. Climate Change: Global Sea Level. National Oceanic and Atmospheric Administration. Available online: https://www.climate.gov/news-features/understanding-climate/climate-change-global-sea-level (accessed on 26 June 2026).
8. Parkinson, R.W.; Wdowinski, S. Geomorphic response of the Georgia Bight coastal zone to accelerating sea level rise, southeastern USA. *Coasts* **2024**, *4*, 1–20.
9. U.S. Army Corps of Engineers. *Incorporating Sea Level Change in Civil Works Programs*; ER 1100-2-8162; U.S. Army Corps of Engineers: Washington, DC, USA, 2019.
10. Eslami, M.M.; Eslami, A. Seawall case studies and failure analysis of sloped concrete walls under static and dynamic loads. *Mar. Georesour. Geotechnol.* **2018**, *36*, 331–339.

11. Loarte, J.S.; Sohrabi, M. Crack Propagation in Concrete Dams Driven by Internal Water Pressure. Master's Thesis, KTH Royal Institute of Technology, Stockholm, Sweden, 2017.
12. ACI Committee 446. *Fracture Mechanics of Concrete: Concepts, Models and Determination of Material Properties*; ACI Committee 446 State-of-the-Art Report; American Concrete Institute: Farmington Hills, MI, USA, 1992.
13. U.S. Army Corps of Engineers. *Evaluation and Repair of Concrete Structures; Engineer Manual EM 1110-2-2002*; Department of the Army: Washington, DC, USA, 1995. Available online: https://www.publications.usace.army.mil/Portals/76/Publications/EngineerManuals/EM_1110-2-2002.pdf (accessed on 27 October 2026).
14. U.S. Army Corps of Engineers. *Gravity Dam Design; Engineer Manual EM 1110-2-2200*; Department of the Army: Washington, DC, USA, 1995. Available online: https://www.publications.usace.army.mil/Portals/76/Publications/EngineerManuals/EM_1110-2-2200.pdf (accessed on 27 October 2026).
15. Ulfkjær, J.P. Fracture Mechanics of Concrete. Ph.D. Thesis, Aalborg University, Aalborg, Denmark, 1992.
16. Zhao, W.; Fang, T.; Chen, X.; Sun, L. Experimental study on hydraulic fracture behavior of concrete with wedge-splitting testing. *Sci. Eng. Compos. Mater.* **2023**, *30*, 20220182. https://doi.org/10.1515/secm-2022-0182.
17. Hakimzadeh, M.; Walkington, N.; Mora-Corral, C.; Gazonas, G.; Dayal, K. Crack Face Contact Modeling Is Essential to Predict Crack-Parallel Stresses. *J. Appl. Mech.* **2025**, *92*, 091006. https://doi.org/10.1115/1.4068510.
18. Siva Parvathi, I.; Mahesh, M.; Raj Kamal, D.V.V. Critical crack lengths of concrete gravity dam by using fracture mechanics. *Mater. Today Proc.* **2021**, *38*, 3149–3159.
19. Ramadan, M.; Jia, J.; Zhao, L.; Li, X.; Wu, Y. Numerical and fracture mechanical evaluation of safety monitoring indexes and crack resistance in high RCC gravity dams under hydraulic fracture risk. *Materials* **2025**, *18*, 2893.
20. Wu, Z.; Rong, H.; Zheng, J.; Dong, W. Numerical method for mixed-mode I-II crack propagation in concrete. *J. Eng. Mech.* **2013**, *139*, 1530–1538.
21. Silarom, K.; Yamamoto, Y. The reproduction ability of a numerical model for simulating the outflow rate of backfilling materials from a coastal structure. *J. Mar. Sci. Eng.* **2019**, *7*, 447.
22. Rambabu, N.; Srineash, V.K. Numerical investigation on the hydrodynamics of vertical seawalls defended by a submerged breakwater. *J. Waterw. Port Coast. Ocean Eng.* **2025**, *151*, 04024020.
23. Miyazaki, N.; Ikeda, T.; Munakata, T. Stress intensity factor analysis by combination of boundary element and finite element methods. *Eng. Fract. Mech.* **1990**, *36*, 61–70.
24. Aour, B.; Rahmani, O.; Nait-Abdelaziz, M. A coupled FEM/BEM approach and its accuracy for solving crack problems in fracture mechanics. *Int. J. Solids Struct.* **2007**, *44*, 2523–2539. https://doi.org/10.1016/j.ijsolstr.2006.08.001.
25. Su, C.; Cai, K.; Xu, Z. A SFBEM-FEM coupling method for solving crack problems based on Erdogan fundamental solutions. *J. Eng. Math.* **2023**, *138*, 3. https://doi.org/10.1007/s10665-022-10247-2.
26. Zhang, L.; Adey, R.A. Coupled FEM-BEM crack growth analysis. In *Boundary Elements and Other Mesh Reduction Methods XXIX*; WIT Transactions on Modelling and Simulation; WIT Press: Southampton, UK, 2007; Volume 44, pp. 267–276. Available online: https://www.witpress.com/Secure/elibrary/papers/BE07/BE07026FU1.pdf (accessed on 27 October 2026).
27. Zhou, L.; Li, C.; Zheng, H. Symmetric positive definite coupling of boundary element method and finite element method: A case study of 2D elastic static problems. *Symmetry* **2026**, *18*, 666. https://doi.org/10.3390/sym18040666.
28. Mukhtar, F.; El-Tohfa, A. A review on fracture propagation in concrete: Models, methods, and benchmark tests. *Eng. Fract. Mech.* **2023**, *281*, 109100.
29. Bažant, Z.P.; Planas, J. *Fracture and Size Effect in Concrete and Other Quasibrittle Materials*; CRC Press: Boca Raton, FL, USA, 1998.
30. Plizzari, G.A. LEFM applications to concrete gravity dams. *J. Eng. Mech.* **1997**, *123*, 808–815. https://doi.org/10.1061/(ASCE)0733-9399(1997)123:8(808).
31. Rankine, W.J.M. On the stability of loose earth. *Philos. Trans. R. Soc. Lond.* **1857**, *147*, 9–27.
32. Xiong, C.; Li, Y.; Wang, Z.; Chen, J. Study on active earth pressure of narrow backfill of balance weight retaining wall. *Undergr. Space* **2024**, *15*, 100–113.
33. Logan, D.L. *A First Course in the Finite Element Method*, 4th ed.; Thomson: Toronto, ON, Canada, 2007.
34. Barsoum, R.S. On the use of isoparametric finite elements in linear fracture mechanics. *Int. J. Numer. Methods Eng.* **1976**, *10*, 25–37.
35. Alshoaibi, A.M.; Fageehi, Y.A. A robust adaptive mesh generation algorithm: A solution for simulating 2D crack growth problems. *Materials* **2023**, *16*, 6481. https://doi.org/10.3390/ma16196481.
36. Alshoaibi, A.M.; Fageehi, Y.A. Simulation of quasi-static crack propagation by adaptive finite element method. *Metals* **2021**, *11*, 98.

37. Xie, G.; Zhou, F. A generation of special triangular boundary element shape functions for 3D crack problems. *Math. Probl. Eng.* **2020**, *2020*, 4629761. https://doi.org/10.1155/2020/4629761.
38. Brebbia, C.A.; Dominguez, J. *Boundary Elements: An Introductory Course*; Computational Mechanics Publications and McGraw-Hill: Southampton, UK, 1992.
39. Saeed, H.; Vancoillie, R.; Mehri Sofiani, F.; De Waele, W. Mode I stress intensity factor solutions for cracks emanating from a semi-ellipsoidal pit. *Materials* **2024**, *17*, 4777. https://doi.org/10.3390/ma17194777.
40. Henshell, R.D.; Shaw, K.G. Crack tip finite elements are unnecessary. *Int. J. Numer. Methods Eng.* **1975**, *9*, 495–507. https://doi.org/10.1002/nme.1620090302.
41. Alshoaibi, A.M.; Fageehi, Y.A. An automated adaptive finite element methodology for 2D linear elastic fatigue crack growth simulation. *Comput. Model. Eng. Sci.* **2025**, *145*, 189-214 https://doi.org/10.32604/cmes.2025.071583.
42. Brebbia, C.A.; Georgiou, P. Combination of boundary and finite elements in elastostatics. *Appl. Math. Model.* **1979**, *3*, 212–220. https://doi.org/10.1016/0307-904X(79)90053-2.
43. Zhu, N.; Oterkus, E. Calculation of stress intensity factor using displacement extrapolation method in peridynamic framework. *J. Mech.* **2020**, *36*, 235–243. https://doi.org/10.1017/jmech.2019.62.
44. Khalid, I.; Qureshi, Z.A.; Ali, H.Q.; Oterkus, S.; Oterkus, E. Structural health monitoring of precracked structures using an in-plane inverse crack-tip element. *Int. J. Mech. Syst. Dyn.* **2024**, *4*, 406–426. https://doi.org/10.1002/msd2.12136.
45. Rice, J.R. A path independent integral and the approximate analysis of strain concentration by notches and cracks. *J. Appl. Mech.* **1968**, *35*, 379–386. https://doi.org/10.1115/1.3601206.
46. Li, F.Z.; Shih, C.F.; Needleman, A. A comparison of methods for calculating energy release rates. *Eng. Fract. Mech.* **1985**, *21*, 405–421. https://doi.org/10.1016/0013-7944(85)90029-3.
47. Raju, I.S.; Shivakumar, K.N. An equivalent domain integral method in the two-dimensional analysis of mixed-mode crack problems. *Eng. Fract. Mech.* **1990**, *37*, 707–725. https://doi.org/10.1016/0013-7944(90)90070-W.
48. Qiao, Y.; Zhang, Z.-X.; Zhang, S. An Experimental Study of the Relation between Mode I Fracture Toughness, K_{IC}, and Critical Energy Release Rate, G_{IC}. *Materials* **2023**, *16*, 1056. https://doi.org/10.3390/ma16031056.
49. Raeisi, R.; Rezaie, F.; Aliha, M.R.M. Mixed-mode I/II and I/III fracture toughness investigation for preplaced aggregate concrete mixtures. *Fatigue Fract. Eng. Mater. Struct.* **2024**, *47*, 2873–2887. https://doi.org/10.1111/ffe.14328.
50. Anderson, T.L. *Fracture Mechanics: Fundamentals and Applications*, 3rd ed.; CRC Press: Boca Raton, FL, USA, 2005.
51. Kanninen, M.F.; Popelar, C.H. *Advanced Fracture Mechanics*; Oxford University Press: New York, NY, USA, 1985.
52. Ma, M.-H.; Wu, Z.-M.; Zheng, J.-J.; Wang, Y.-J.; Yu, R.C.; Fei, X.-D. Effect of loading rate on mixed mode I-II crack propagation in concrete. *Theor. Appl. Fract. Mech.* **2021**, *112*, 102916.10.1016/j.tafmec.2021.102916.
53. Hua, W.; Li, J.; Zhu, Z.; Li, A.; Huang, J.; Gan, Z.; Dong, S. A review of mixed mode I-II fracture criteria and their applications in brittle or quasi-brittle fracture analysis. *Theor. Appl. Fract. Mech.* **2023**, *124*, 103741. https://doi.org/10.1016/j.tafmec.2022.103741.

Disclaimer/Publisher's Note: The statements, opinions and data contained in all publications are solely those of the individual author(s) and contributor(s) and not of MDPI and/or the editor(s). MDPI and/or the editor(s) disclaim responsibility for any injury to people or property resulting from any ideas, methods, instructions or products referred to in the content.